EXPRES. II. Searching for Planets around Active Stars: A Case Study of HD 101501

Samuel H. C. Cabot[1] , Rachael M. Roettenbacher[2] , Gregory W. Henry[3] , Lily Zhao[1] , Robert O. Harmon[4],
Debra A. Fischer[1] , John M. Brewer[5] , Joe Llama[6] , Ryan R. Petersburg[1] , and Andrew E. Szymkowiak[1]

[1] Yale University, 52 Hillhouse Avenue, New Haven, CT 06511, USA; sam.cabot@yale.edu
[2] Yale Center for Astronomy and Astrophysics, Yale University, 46 Hillhouse Avenue, New Haven, CT 06511, USA
[3] Tennessee State University, Center of Excellence in Information Systems, Nashville, TN 37203, USA
[4] Ohio Wesleyan University, 61 S. Sandusky Street, Delaware, OH 43015, USA
[5] Department of Physics and Astronomy, San Francisco State University, 1600 Holloway Avenue, San Francisco, CA 94132, USA
[6] Lowell Observatory, 1400 W. Mars Hill Road, Flagstaff, AZ 86001, USA

Abstract

By controlling instrumental errors to below $10\,\mathrm{cm\,s^{-1}}$, the EXtreme PREcision Spectrograph (EXPRES) allows for a more insightful study of photospheric velocities that can mask weak Keplerian signals. Gaussian processes (GP) have become a standard tool for modeling correlated noise in radial velocity data sets. While GPs are constrained and motivated by physical properties of the star, in some cases they are still flexible enough to absorb unresolved Keplerian signals. We apply GP regression to EXPRES radial velocity measurements of the 3.5 Gyr old chromospherically active Sun-like star, HD 101501. We obtain tight constraints on the stellar rotation period and the evolution of spot distributions using 28 seasons of ground-based photometry, as well as recent Transiting Exoplanet Survey Satellite data. Light-curve inversion was carried out on both photometry data sets to reveal the spot distribution and spot evolution timescales on the star. We find that the $>5\,\mathrm{m\,s^{-1}}$ rms radial velocity variations in HD 101501 are well modeled with a GP stellar activity model without planets, yielding a residual rms scatter of $45\,\mathrm{cm\,s^{-1}}$. We carry out simulations, injecting and recovering signals with the GP framework, to demonstrate that high-cadence observations are required to use GPs most efficiently to detect low-mass planets around active stars like HD 101501. Sparse sampling prevents GPs from learning the correlated noise structure and can allow it to absorb prospective Keplerian signals. We quantify the moderate to high-cadence monitoring that provides the necessary information to disentangle photospheric features using GPs and to detect planets around active stars.

Unified Astronomy Thesaurus concepts: Exoplanet detection methods (489); Radial velocity (1332); Gaussian Processes regression (1930)

1. Introduction

Radial velocity (RV) measurements have yielded numerous detections of exoplanetary systems via the gravitational interactions between planets and their host stars. In parallel, we have gained a deeper understanding of stellar physics and exoplanet populations. The improved technological capability of the latest generation of spectrographs enables the search for Earth analogues orbiting nearby stars in our Galaxy. One such observing program focuses on near-infrared (NIR) observations of M dwarfs with the Calar Alto high-Resolution search for M dwarfs with Exoearths with Near-infrared and optical Échelle Spectrographs (CARMENES) spectrograph (Quirrenbach et al. 2010); others observe low-mass stars in the optical using ultra-stable spectrographs such as the Echelle SPectrograph for Rocky Exoplanets and Stable Spectroscopic Observations (ESPRESSO; Pepe et al. 2013; Suárez Mascareño et al. 2020) or EXtreme PREcision Spectrometer (EXPRES; Jurgenson et al. 2016; Blackman et al. 2020; Petersburg et al. 2020). Solar or subsolar mass stars are desirable RV targets because they exhibit greater reflex velocities from orbiting exoplanets. However, these host stars also have convective outer layers that contribute nuisance signals in RV time-series data. Along with high instrumental precision, it is of paramount importance to disentangle the Keplerian RV signal of an exoplanet from stellar activity signals.

Significant effort has been dedicated toward theoretical or empirical modeling of the stellar activity RV contribution. One example is a simple spot model (Aigrain et al. 2012), which estimates the RV signature based on simultaneous photometric monitoring. Recent studies employ quasiperiodic Gaussian processes (GPs) and moving-average methods to capture more complex correlated noise in RV time series (Tuomi et al. 2013; Haywood et al. 2014). These techniques force the model to be correlated on specific timescales, but uncorrelated after a parameterized decay timescale. Stellar activity may be probed, in part, by certain indicators and proxies derived from spectra. The cross-correlation function (CCF) between a stellar spectrum and model template provides a couple of indicators (Queloz et al. 2001, 2009). For example, the bisector inverse slope (BIS; Toner & Gray 1988) probes granulation blueshift as a function of increasing height in the photosphere. Spots break the symmetrical, rotationally broadened line profile as they move across the stellar surface, and produce variations in the CCF FWHM (Figueira et al. 2013). Emission in cores of calcium II H&K lines (denoted $\log R'_{\rm HK}$) probes chromospheric activity (Saar et al. 1998; Cincunegui et al. 2007). The Hα core equivalent width is correlated with the overall photometric flux and used as a proxy in the simple spot model (Giguere et al. 2016). Stellar activity may also be isolated by its impact on individual lines (Davis et al. 2017; Dumusque 2018; Cretignier et al. 2020). However, despite these diagnostic advances, there is no robust methodology for consistently distinguishing low-mass planetary signals from stellar activity in RV data sets (Dumusque et al. 2017).

Higher fidelity data acquired by new state-of-the-art spectrographs can reach $\lesssim 30\,\mathrm{cm\,s^{-1}}$ measurement precision (Brewer et al. 2020; Suárez Mascareño et al. 2020) and might hold clues

to solving this longstanding problem. We thus turn our attention to HD 101501 (61 UMa), which provides an exemplary case of stellar activity that dominates an RV time series. The star is bright ($V = 5.31$) and Sun-like (G8V; Boyajian et al. 2012) and is a target in the EXPRES observing program (Brewer et al. 2020). Historically, the star has been used as a standard for spectral classification of stars (Johnson & Morgan 1953) and is commonly included in population studies of Sun-like stars (Duquennoy & Mayor 1991; Fischer & Valenti 2005; Valenti & Fischer 2005). HD 101501 has a rotation period of ∼16 days (Donahue et al. 1996) and no confirmed companions. Fischer et al. (2014) published RVs for HD 101501 from the Lick Observatory Hamilton spectrograph with an rms of 13.48 m s^{-1} and Howard & Fulton (2016) show a similar rms of 13.12 m s^{-1} from combined Lick and Keck data. This RV scatter is large enough to mask Keplerian signals of planets with mass $\lesssim 100\,M_\oplus$. Active, young stars are usually off limits for RV observing programs, which explains the lack of HD 101501 observations in the High Accuracy Radial Velocity Planet Searcher (HARPS) or HARPS-N archival databases. However, these properties make the star a fascinating case study for in-depth characterization, as well as a testbed for methods which reduce correlated RV noise.

As follows we present new high-precision RVs of HD 101501 with simultaneous photometry. Details regarding the data are in Section 2. We employ GPs for modeling stellar activity. In Section 3 we review the GP method and its application to our data set, as well as present benchmarks on archival data. Section 4 contains the results of our planet search of HD 101501, in which we compare multiple GP-based models and find that an activity-only (zero planet) model has the highest evidence. One of the limitations of the RV data is seasonal low cadence over certain stretches of time, which hinders the GP from learning activity signals and distinguishing them from possible short-period Keplerians. We quantify the impact of cadence in Section 5 and recommend observing strategies for detecting planets around active stars. We find that high cadence is necessary for using GPs to detect low-amplitude planets around HD 101501 and other active stars. We perform a detailed characterization of stellar rotation and activity in Section 6 by performing light-curve inversion. Section 6.4 summarizes our results.

2. Observations

Our data consist of high-precision RV measurements and simultaneous ground-based photometry. This combination is advantageous because it allows joint constraints on stellar activity between the two time series (Haywood et al. 2014). Details surrounding data acquisition and processing are as follows. We also analyze photometry from the Transiting Exoplanet Survey Satellite (TESS), which partially overlaps the recent EXPRES RV data.

2.1. Photometry with APT

Fairborn Observatory's Automatic Photoelectric Telescopes (APTs; Henry 1999) observed HD 101501 for 28 seasons (spanning 1993 April 18–2020 June 21). Observations have about 1 day typical cadence for 6–7 months each year, totalling 2673 data points. The data display a significant correlated structure arising from stellar activity in the target and have a

standard deviation of 7.1 mmag in the V band. We focus on activity from spots, which are modulated by the rotational period, and remove long-term brightness variations from the light curve. The long-term trend of the light curve that cannot be simply attributed to rotational modulation is removed by smoothing the light curve over 100 days and subtracting the resultant trend. The light-curve standard deviation is reduced to 4.5 mmag, following detrending (Figure 1). The periodogram has complex structure around 17 days, close to the 16.18 day rotation period estimated by Donahue et al. (1996). The maximum power is at 17.51 days.

2.2. Photometry with TESS

TESS (Ricker et al. 2014) observed HD 101501 during Sector 22 (2020 February 18–2020 March 18; Figure 2). The 2 minute cadence, simple aperture photometry (SAP) light curve was used and the first five cotrending basis vectors were applied to remove instrumental signatures in order to preserve stellar astrophysics (following the process used in Roettenbacher & Vida 2018). Both the light curve and cotrending basis vectors were obtained through the Barbara A. Mikulski Archive for Space Telescopes (MAST).

2.3. Spectroscopy with EXPRES

We analyze 76 RVs (over 33 distinct nights) of HD 101501 obtained between 2018–2020. Data were collected with EXPRES commissioned at the 4.3 m Lowell Discovery Telescope (Levine et al. 2012; observing program: The 100 Earths Survey). EXPRES achieves ∼30 cm s^{-1} measurement precision for a pixel signal-to-noise ratio of 250 at 5500 Å. EXPRES has typical resolving power of $R \sim 137,500$ and spans a wavelength range of 380–780 nm. More details regarding EXPRES may be found in recent studies investigating performance benchmarks and detailing the RV extractions (Blackman et al. 2020; Brewer et al. 2020; Petersburg et al. 2020). We also extract activity indicators (CCF FWHM, CCF BIS, and Hα equivalent width) for each exposure, derived from the spectrum and CCF. The 100 Earths Survey targets chromospherically quiet stars without close-in gas giants in order to search for terrestrial planets. HD 101501 represents one of several additional, active stars observed for purposes of investigating and mitigating activity signals. Physical attributes of HD 101501 are listed in Table 1, and summary statistics for the EXPRES exposures are in Table 2. For convenience, we subtract the mean of the RV data (about -5.55 km s^{-1}) corresponding to the systemic velocity.

3. GP for Modeling Stellar Activity

Before describing the GP framework, we review physical processes within the star that are responsible for RV variations. They may be categorized as follows (Dumusque et al. 2012; Fischer et al. 2016; Cegla 2019): (1) p-mode acoustic oscillations in the convective envelope (Chaplin & Miglio 2013) induce RV variations of order $\lesssim 1$ m s^{-1} on timescales of several minutes. Observing strategies can often average out and reduce this effect to within the instrument precision (Dumusque et al. 2011). (2) Granulation cells consist of rising hot gas and descending cool gas. Depending on the temperature of the gas, granulation induces a net blueshift (Dravins 1982) and variability of tens of cm s^{-1} (Schrijver & Zwaan 2000) over the course of several minutes. (3) Magnetic activity cycles like the solar cycle inhibit
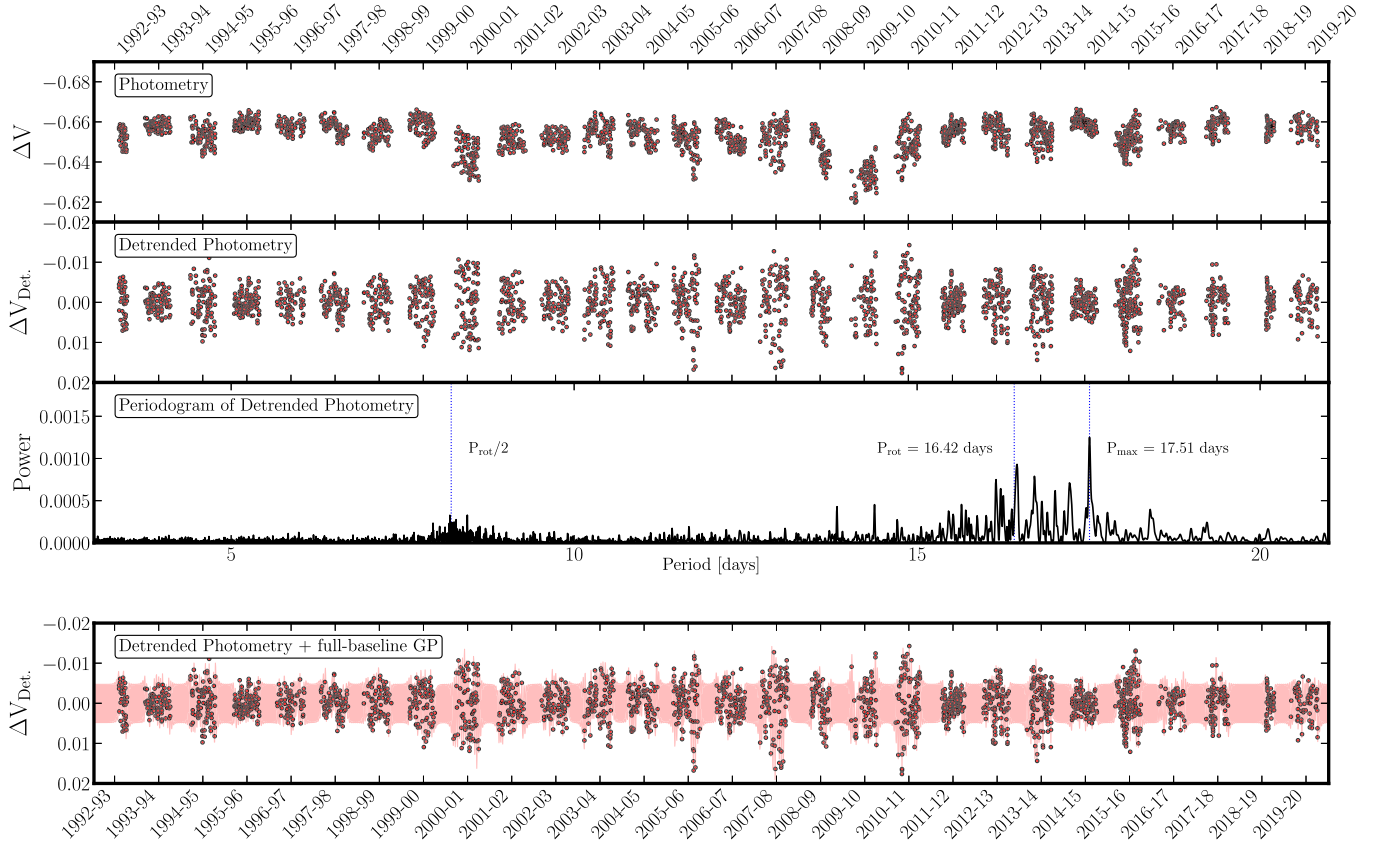
Figure 1. Full APT photometry data set providing *V*-band monitoring of HD 101501. Top panel: data set in units of relative magnitude. Second panel: data set following the detrending procedure described in the text. Long-term variations are removed. The scatter within each season reflects stellar activity modulated by the rotation period. Third panel: generalized Lomb–Scargale periodogram of the detrended photometry. We mark the period of maximum power P_{max}, our determined rotational period P_{rot} (see Section 6), and $P_{\mathrm{rot}}/2$. Bottom panel: detrended photometry plotted with the full-baseline, `celerite`, quasiperiodic GP fit. The red band is the 1σ confidence interval of the GP. We infer the rotation period of the star as the maximum a posteriori value of the GP periodic timescale parameter, $P_{\mathrm{rot}} = P_{\mathrm{GP}}$ (details in Section 6).

the convective blueshift (Meunier & Lagrange 2013), typically on timescales of years. (4) Spots and faculae can create especially pernicious RV variations with amplitudes and periods commensurate with planetary signals (Boisse et al. 2011). The magnetic fields associated with spots and faculae inhibit convection in local regions on the star. The effect is modulated by the stellar rotation, and therefore can be confused for an exoplanet with an orbital period at a harmonic of the stellar rotation period (Queloz et al. 2001), especially in undersampled RV data sets. Starspot lifetimes vary from days to years (Hall & Henry 1994; Berdyugina 2005) and hence induce a quasiperiodic RV variation. In some cases, the sinusoidal variation remains coherent over several months (Robertson et al. 2020).

3.1. GP Formalism

The stochastic nature of stellar activity makes it difficult to model analytically, and has motivated the use of GPs (Haywood et al. 2014; Rajpaul et al. 2015). A GP is a flexible model which assumes that data points are drawn from a multivariate normal distribution (Rasmussen & Williams 2006). Under a GP model, RV measurements y at times t have the joint distribution

$$p(\boldsymbol{y}; \boldsymbol{t}) \sim \mathcal{N}(m(\boldsymbol{t}), K(\boldsymbol{t}, \boldsymbol{t}) + \sigma_n^2 I), \qquad (1)$$

where m is a mean function and K is a covariance matrix. The mean and covariance functions have hyperparameter vectors θ

and ϕ, respectively. The white noise term involves measurement uncertainties σ_n. GPs can serve as predictive models for estimating values and uncertainties at times between measurements. The agreement between a GP model and observed data may be quantified by the logarithm of the marginal likelihood

$$\log \mathcal{L}(\theta, \phi) = -\frac{1}{2} \boldsymbol{r}^\top (K + \sigma_n^2 I)^{-1} \boldsymbol{r}$$
$$- \frac{1}{2} \log |K + \sigma_n^2 I| - \frac{n}{2} \log 2\pi, \qquad (2)$$

where the vector of residuals is

$$\boldsymbol{r} = \boldsymbol{y} - m(\boldsymbol{t}). \qquad (3)$$

GPs have been used extensively in the literature for modeling correlated noise in RV data sets, and enabling detections of low-mass planets (e.g., Haywood et al. 2014; Grunblatt et al. 2015; Rajpaul et al. 2015; Cloutier et al. 2017; Benatti et al. 2020; Faria et al. 2020; Suárez Mascareño et al. 2020). In these cases, m as defined above takes the form of a Keplerian signal or sum of multiple Keplerians. The Keplerians increase $\log \mathcal{L}(\theta, \phi)$ by decreasing the residuals in $\boldsymbol{r}$ and changing the optimal hyperparameters. Some restrictions in the GP framework make it more appropriate for modeling stellar noise in RV data sets, and prevent it from absorbing planetary signals;
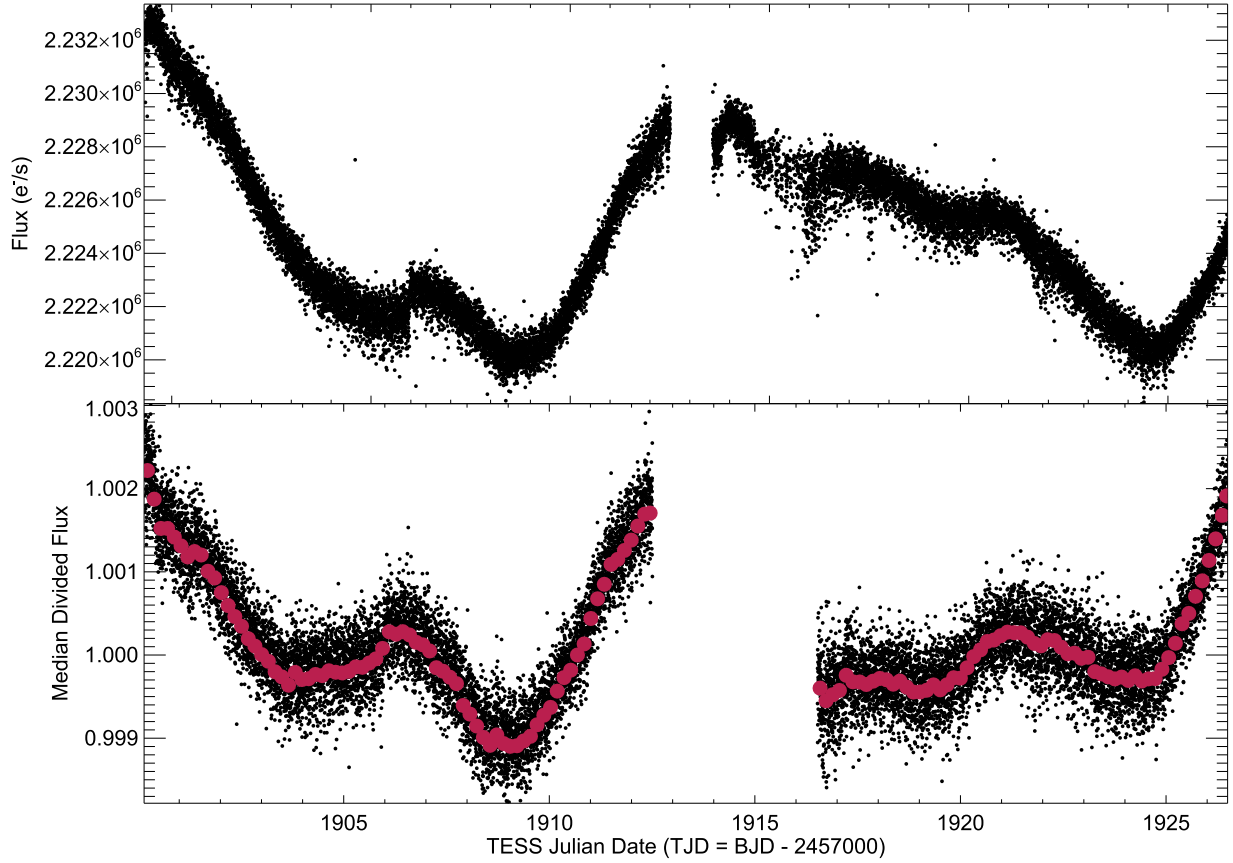
Figure 2. Sector 22 TESS light curve. Top: the 2 minute SAP light curve provided by the standard TESS pipeline. Bottom: the TESS light curve with the first five cotrending basis vectors removed. Plotted in red are the average flux values for the binned light curve used by in our inversions, see Section 6.3. When used in the inversions, these fluxes are normalized for each rotation, here they are overlaid for comparison.

Table 1
Physical Properties of HD 101501

Property	Symbol	Units	Value[a]
Visual Magnitude	V	mag.	5.31
Distance	d	pc	9.61
Effective Temperature	$T_{\rm eff}$	K	5502
Surface Gravity	$\log g$	cm s^{-2}	4.52
Metallicity	[Fe/H]	[Fe/H]$_\odot$	-0.04
Age	$t_{\rm age}$	Gyr.	$3.5^{+2.8}_{-2.2}$
Proj. Rotation Speed	$v \sin i$	km s^{-1}	2.2
Luminosity	$\log L_*$	$\log L_\odot$	-0.21 ± 0.02
Radius	R_*	$R_\odot$	0.86 ± 0.02
Mass	M_*	$M_\odot$	0.90 ± 0.12

Note.
[a] All values and uncertainties are as reported by Brewer et al. (2016).

Table 2
Summary of EXPRES Radial Velocity Measurements Used in This Study

Property	Symbol	Units	Value
Number of Exposures	$N_{\rm exp}$	⋯	76
Number of Nights	$N_{\rm night}$	⋯	33
Time Baseline	⋯	days	796
Average RV	$\widehat{RV}$	m s^{-1}	-5554.43
RV rms	rms	m s^{-1}	6.1
Median Measurement Uncertainty	$\tilde\sigma_n$	m s^{-1}	0.38

namely, a quasiperiodic covariance function

$$K_{ij} = a^2 \exp\left[-\frac{|t_i - t_j|^2}{\lambda_e^2} - \frac{\sin^2(\pi|t_i - t_j|/P_{\rm GP})}{\lambda_p^2}\right], \quad (4)$$

which is the product of squared-exponential and sinusoidal covariance functions. The hyperparameters $\phi = \{a^2, \lambda_e, \lambda_p, P_{\rm GP}\}$ correspond to the magnitude of covariance, a decay parameter for the overall GP evolution, a dimensionless smoothing parameter for the periodic component, and the period of oscillations, respectively. This choice is motivated by the underlying physics when $P_{\rm GP}$ equals $P_{\rm rot}$, the rotation period of the star, and λ_e is related to the typical lifetimes of spots; however direct interpretations of hyperparameters beyond the rotation period are tenuous (Rajpaul et al. 2015). Often a jitter parameter s is added in quadrature with measurement uncertainties (Grunblatt et al. 2015). Foreman-Mackey et al. (2017) show the covariance function,

$$K_{ij} = \frac{B}{2+C} e^{-|t_i - t_j|/L} \left[\cos\frac{2\pi|t_i - t_j|}{P_{\rm GP}} + (1 + C)\right], \quad (5)$$

behaves similar to Equation (4), and allows faster matrix inversion (Equation (2)). It has been used in recent RV studies (Robertson et al. 2020; Suárez Mascareño et al. 2020) and compared to other available kernels (Espinoza et al. 2020). Hyperparameters $\phi = \{B, C, L, P_{\rm GP}\}$ correspond to the

magnitude of covariance, weighting of the sinusoidal term, decay parameter, and period, respectively. Most studies which use GPs to model correlated RV noise adopt one of the above two covariance functions, and for our analyses we use the `george` implementation (Ambikasaran et al. 2015) for Equation (4) and the `celerite` implementation (Foreman-Mackey et al. 2017) for Equation (5). We briefly note a few differences between the kernels. The `celerite` GP is not mean-square differentiable (Rasmussen & Williams 2006) and is less smooth than the `george` GP. Also the covariance decreases faster on short timescales compared to the `george` GP for equal $\lambda_e = L$. RV variations due to the star are stochastic on many different timescales and are not necessarily a smooth or coherent process. However, the actual power spectrum of high-frequency variations will depend on the RV signatures of granulation and oscillations, which are not well understood. Given its smoothness, Equation (4) is a more attractive model for activity associated with faculae and spots, which themselves evolve on timescales comparable to the rotation period. We applied the GP framework with both kernels on the identical CoRoT-7 data set analyzed by Faria et al. (2016). The GP + two-planet model favored use of the `george` GP over the `celerite` GP with $\Delta \ln \mathcal{Z} \approx 8$ (this metric is described in the following subsection). In both cases we found that the sampler tended to converge to an alias of the 0.85 day period planet at ~6 days, but that the shorter period planet is visible in the residuals and periodogram following subtraction of the 3.7 day planet and GP. The correct orbital period was retrieved after imposing a prior restricted to orbital periods of $P < 5$ days. Figure 3 shows our best fit. Moving forward we adopt the `george` GP for modeling RV noise.

3.2. Application to EXPRES RVs and APT Light Curve

We couple the GP framework with the importance nested sampling algorithm `MultiNest` (Feroz & Hobson 2008; Feroz et al. 2009, 2019) via the `PyMultiNest` implementation (Buchner et al. 2014). The parameter space includes GP hyperparameters $\{a^2, \lambda_e, \lambda_p, P_{GP}\}$, jitter parameter s, systemic offset γ, and orbital parameters $\{K_s, \phi_0, P, \omega, e\}$ for N planets, corresponding to semi-amplitude, phase of first epoch, orbital period, longitude of periastron, and eccentricity, respectively. We adopt ϕ_0 as a boundary condition instead of time of periastron (T_p) since there are no degeneracies in the $[0, 2\pi]$ prior. `MultiNest` returns the log evidence of the model, $\ln \mathcal{Z}$, which may be used for model comparison for $N = \{0, 1, 2, 3, ...\}$ planets. Given data set $\boldsymbol{d}$ and a model $\mathcal{M}$ parameterized by a vector θ, the Bayesian evidence is defined as

$$\mathcal{Z} \equiv p(\boldsymbol{d}|\mathcal{M}) = \int p(\boldsymbol{d}|\boldsymbol{\theta}, \mathcal{M}) p(\boldsymbol{\theta}|\mathcal{M}) d\boldsymbol{\theta} \qquad (6)$$

(Bayesian evidence in the context of RV analyses is discussed at length by Nelson et al. 2020). Assuming equal prior odds on given models $\mathcal{M}_0$ and $\mathcal{M}_1$ (e.g., zero planets and one planet, respectively), it is generally agreed that a difference in corresponding evidences $\ln \mathcal{Z}_1 - \ln \mathcal{Z}_0 \geqslant 5$ indicates that $\mathcal{M}_1$ is strongly preferred over $\mathcal{M}_0$ (Kass & Raftery 1995). Our model evidences and uncertainties correspond to the median and standard deviation of evidences from five runs of the sampler. Repeated runs are known to provide more reliable
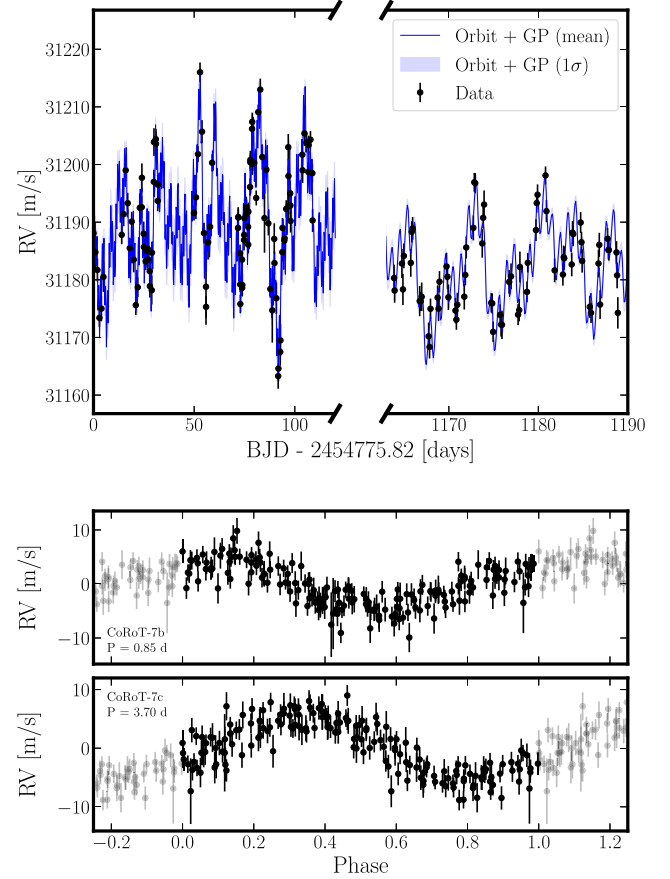

Figure 3. The orbits of CoRoT-7b and CoRoT-7c, retrieved by applying the `george` quasiperiodic GP + two-planet model to RV observations of the system. These detections are made on the same data set analyzed by Faria et al. (2016), and are consistent with their results, as well as results presented by Haywood et al. (2014). The top panel shows the data and best-fit model, including the GP 1σ confidence interval. The bottom panels show, for each planet, the phase-folded orbit after subtracting the other planet's orbit and GP mean.

uncertainty estimates than single-run output (Nelson et al. 2020). Our choices of priors are listed in Table 3. The priors on orbital parameters represent our expectations for what could be detected in the data, given the sparse sampling and large fluctuations.

We perform a similar analysis as Haywood et al. (2014) by conditioning GP hyperparameters based on simultaneous photometry. We fit a `george` GP model to the most recent three seasons of photometry (2018–2020), including a jitter parameter and constant offset. Note, the matrix inversion becomes intractable for many data points, so we restrict this step to the timeframe overlapping with EXPRES RV observations, neglecting pre-2018 data. We use log-uniform priors spanning multiple orders of magnitude on all parameters with two exceptions: the constant offset is drawn from a uniform prior, and the periodic timescale is bounded by 12 days and 22 days. This latter constraint was chosen to prevent convergence on a harmonic or multiple of the rotation period. Afterwards, when we use a GP model to fit the RVs, the hyperparameters λ_e, λ_p, and P_{GP} are fixed to the maximum a posteriori (MAP) values from photometry fitting. The amplitude a is allowed to be different. Fixing model parameters decreases the sampling dimensionality and computation time. It

Table 3
Priors on Parameters for the Light-curve-conditioned, One-planet RV Model

Parameter	Definition	Units	Distribution
GP			
a	Amplitude	m s^{-1}	$\mathcal{LU}(0.1, 1000)$
λ_e	Decay Timescale	days	$\delta(18.74)$
$P_{\rm GP}$	Periodic Timescale	days	$\delta(16.28)$
λ_p	Smoothing Parameter	⋯	$\delta(0.76)$
Global			
s	Jitter	m s^{-1}	$\mathcal{U}(0.01, 5)$
γ	Systemic Offset	m s^{-1}	$\mathcal{U}(-20, 20)$
Orbital			
K_s	Semi-amplitude	m s^{-1}	$\mathcal{LU}(0.1, 10)$
ϕ_0	Phase of First Epoch	rad.	$\mathcal{U}(0, 2\pi)$
P	Period	days	$\mathcal{LU}(0.5, 20)$
ω	Longitude of Pericenter	rad.	$\mathcal{U}(0, 2\pi)$
e	Eccentricity	⋯	$\mathcal{LU}(0, 0.99)$

Note. We sample george GP covariance parameters (Equation (4)), global parameters including a jitter term and RV offset, and orbital parameters for a single planet. The table lists each parameter, its corresponding units, and prior distribution. For uniform ($\mathcal{U}$) and log-uniform ($\mathcal{LU}$) distributions, we specify upper and lower bounds. For this model, three of the four GP parameters are fixed (denoted by δ) to values inferred from photometry.

also informs the model in case the RVs alone are insufficient to constrain the stellar rotation period. It is expected that GP fits to RV and photometry time series should have similar λ_e, λ_p, and $P_{\rm GP}$, as demonstrated by Kosiarek & Crossfield (2020) with solar data (see their Figure 9).

4. Results

We now present results of GP model fits to the photometry and RVs, which includes searching for planetary companions around HD 101501.

4.1. Photometric Contraints

In fitting a george GP model to 2018–2020 photometry, we obtain MAP hyperparameter values $a = 3.40$ mmag., $\lambda_e = 18.74$ days, $P_{\rm GP} = 16.28$ days, and $\lambda_p = 0.76$. The george GP with MAP hyperparameters is plotted against the recent photometry data in Figure 4. The joint distributions between GP hyperparameters and their marginalized histograms are shown in Figure 5. All of the hyperparameters are constrained around well-defined peaks. Both λ_e and λ_p have an effect on whether the GP rapidly varies or gradually changes (Rasmussen & Williams 2006). Larger λ_e allows the GP to repeat itself more times before it loses coherence. Larger λ_p forces the repeating signal to be smoother, whereas smaller λ_p allows a more fine structure. While not strictly enforced by our priors, the evolutionary timescale converged to a value larger than the periodic timescale ($\lambda_e > P_{\rm GP}$). This is a realistic constraint in regressing quasiperiodic GPs to photometry (Kosiarek & Crossfield 2020).

4.2. RV Characterization and Planet Search

The zero-planet (GP-only) model is most favored at a log evidence of $\ln \mathcal{Z} = -149.26 \pm 0.15$, compared to the GP +

one-planet model at $\ln \mathcal{Z} = -149.72 \pm 0.06$. We additionally restricted the Keplerian to a sinusoid (circular orbit) by fixing $\omega = 0$ and $e = 0$. This model returned $\ln \mathcal{Z} = -149.75 \pm 0.18$. For the one-planet model, the MAP planet period is at 15.24 days, which is close to the adopted stellar rotation period, whereas the MAP period is at 6.68 days in the sinusoid model. The MAP eccentricity reaches 0.12 in the one-planet model, which also suggests that the Keplerian component is conforming to signals associated with stellar activity and rotation. Fit results for the three models are in Table 4.

We attempted fitting a GP model on RVs without conditioning from photometry. For each of these models we sampled λ_e, λ_p, and $P_{\rm GP}$ from prior distributions $\mathcal{LU}(1, 100)$, $\mathcal{LU}(0.1, 100)$, and $\mathcal{LU}(10, 50)$, respectively ($\mathcal{LU}$ denotes the log-uniform distribution, with lower and upper bounds). Indeed, with appropriate amounts of data, observing cadence, and handling of model evidences, planets and GP noise parameters can be inferred from RVs alone (Faria et al. 2016). The GP-only model yields MAP values of $\lambda_e = 30.44$ days and $P_{\rm GP} = 15.48$ days. The GP + one-planet model returns $\lambda_e = 46.43$ days and $P_{\rm GP} = 15.59$ days. The returned planet has MAP orbital parameters $K_s = 1.1$ m s^{-1} and $P = 2.1$ days. However, the GP-only model is favored at $\Delta \ln \mathcal{Z} \simeq 1$. While the inferred stellar rotation period is consistent with the photometry-derived rotation period, the spot evolution timescale is closer to twice the photometry value, probably due to the sparse sampling of the RV data.

Given that the model evidences are all within $|\Delta \ln \mathcal{Z}| < 2$ of each other, it is difficult to make decisive inferences through their comparison. The points that we would like to emphasize are that: (1) for this data set, conditioning on high-cadence photometry provides important constrains on the stellar activity model that are otherwise difficult to infer from RVs alone, including a more accurate rotation period and spot evolution timescale; (2) consistent with previous analyses of other stars, the spot decay timescale tends to be longer than the stellar rotation period but within the same order of magnitude; and (3) the Bayesian evidence favors an activity model without planets. The GP's flexibility here is crucial since the activity signal quickly loses coherence, and spots follow various rotation periods depending on latitude. Both of these aspects are addressed by choosing a proper λ_e and a single characteristic $P_{\rm GP}$, respectively. In the following section we discuss the temporal sampling of our data, and how observing scheduling can improve the sensitivity of our analysis to short-period signals. In particular, additional high-cadence RVs are necessary to rule out some planets at the $K_s \approx 3$ m s^{-1} level.

5. Importance of Cadence

The RV data set analyzed here presents a combination of fast cadence bursts, as well as isolated data points. The high-amplitude RV variations are well sampled in 2018 (top panel of Figure 6), but more poorly sampled in 2019 and 2020 (middle and bottom panels). Cadence may be less important when Keplerians have higher amplitude than the stellar activity (e.g., hot Jupiters or planets around quiet stars). However, high cadence is very useful when stellar activity dominates the time series, especially for detecting short-period planets. If RVs have cadence longer than spot lifetimes, then it is challenging for the GP model to learn the smoothness or periodicity of the activity signal. Isolated data points (e.g., those acquired in 2020) provide little information in this sense. It is worth
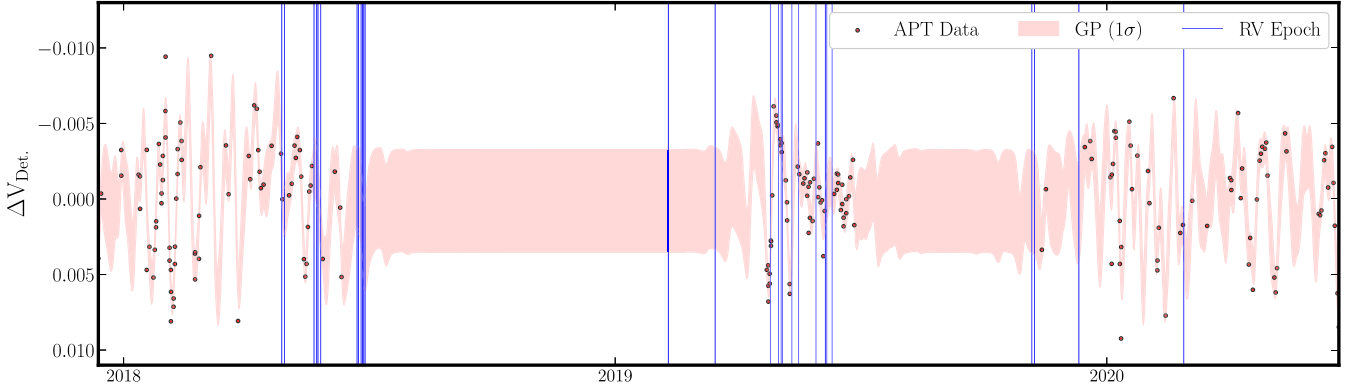
Figure 4. Detrended APT photometry of HD 101501 for 2018, 2019, and 2020 observing seasons. The red shaded region depicts the 1σ confidence region around the regressed `george` GP mean. The blue lines denote epochs of RV measurements.
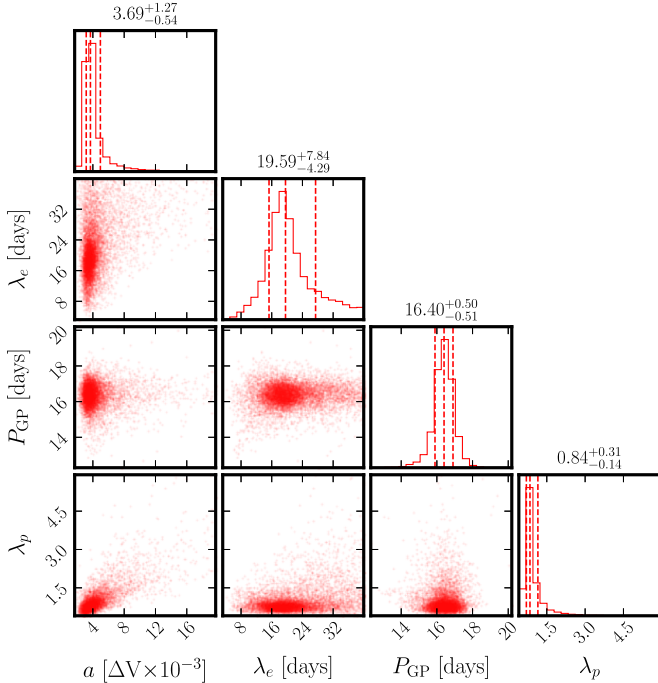

Figure 5. Marginalized posterior distributions of hyperparameters for the `george` GP model regressed to the 2018–2020 APT photometry. Samples were obtained via an importance nested sampling of the posterior distribution, as described in the text. Median values are plotted above the 1D histograms, where uncertainties correspond to 16th and 84th percentiles. These quantiles are marked by red dashed lines.

mentioning the recent discovery of a multiplanet system around GJ 887 (Jeffers et al. 2020). Confident detection was only made possible by a single, high-cadence observing season (∼1 exposure per clear night), even though there were nearly 20 years of existing data (on average ∼11 RVs per year). Another example is the case of Proxima Centauri b, in which one high-cadence observing season led to a higher detection significance than years of previous data (Anglada-Escudé et al. 2016). Optimal cadence has been investigated before in the contexts of averaging out the activity contribution (Dumusque et al. 2011) and its relationship to orbital phase coverage (Rajpaul et al. 2017). Nightly coverage has also been compared to other ground- and space-based schedules (Hall et al. 2018). However, the relationship between observing cadence and GP modeling of activity has not previously been characterized.

5.1. An Injection and Recovery Analysis

To quantify the impact of cadence in our analysis, we perform a simple injection/recovery test as follows. First, we generate a synthetic RV time series by drawing a `george` GP specified by Equation (4), characteristic of our HD 101501 observations. Hyperparameters are set to the MAP values in Section 4.1. The amplitude is set to 5.06 m s^{-1}, which is the the MAP amplitude of the GP-only fit in Section 4.2. Next, we add a Keplerian component with K_s and P sampled from a grid. Other Keplerian parameters are set to zero. We sample the continuous RV curve at 33 epochs (described below) and add random noise drawn from a zero-mean normal distribution with a standard deviation of 40 cm s^{-1}, which is also the associated uncertainty on each data point. Finally, we fit a GP + sinusoidal model as discussed in Section 3 with three GP hyperparameters fixed, as if they had been predetermined by photometry measurements. We then compare the recovered K_s and P to the actual injected signal. Each full run involves a pair (K_s, P) and new GP draw. The sampler is run only once since we are not interested in precise uncertainties on the model evidence. The procedure is illustrated in Figure 7.

The test described above is repeated for several toy observing cadences. We define an N-day cadence as observing for N consecutive nights (separated by one sidereal day), followed by a long gap in time. The gap is drawn from a uniform random distribution between 50 and 80 days. This pattern repeats until the number of exposures totals 33, which was the number of nights HD 101501 was observed by EXPRES at the start of simulations (a couple of additional, recent nights were included in the RV analysis). Each timestamp is then perturbed by a uniformly random variable between -4 and $+4$ hr to simulate variations in observing scheduling. The 50–80 day gap is about 3–5 × λ_e, chosen to destroy coherence between consecutive bursts of exposures. A variable gap helps avoid unwanted sampling artifacts. We repeat the above test for 2, 5, 10, 20, and 33 day cadences. For example, the 5 day cadence involves timestamps for five consecutive nights, followed by a long gap in time. The pattern repeats six times, followed by three exposures such that the number of data points equals 33. The cadences roughly sample 1/8, 1/4, 1/2, 1, and 2 stellar rotations. As a benchmark we also sample at the identical timestamps of EXPRES data. These tests do not encompass sophisticated modeling of stellar noise or the wide variety of observing strategies and possible Keplerian signals (e.g., eccentric orbits, multiple planets).
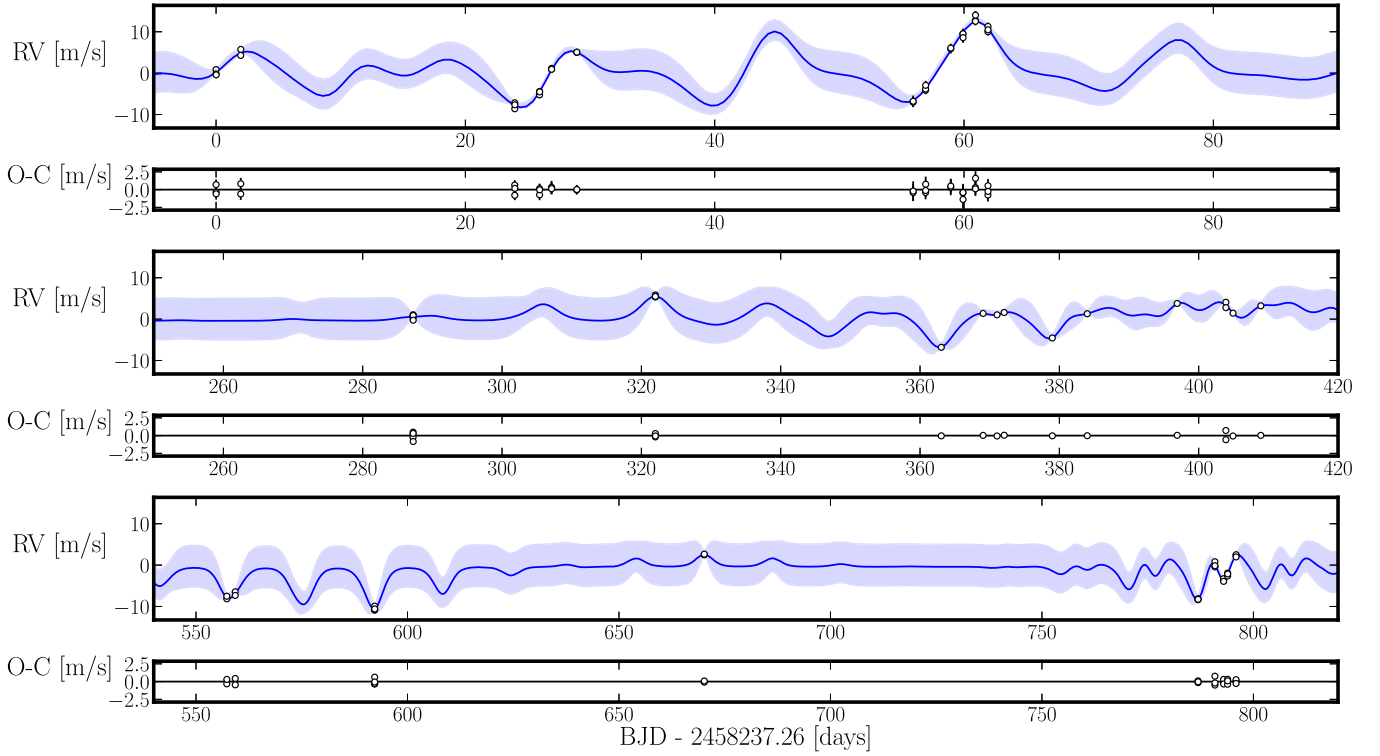
Figure 6. GP-only fit to EXPRES RV measurements of HD 101501. The `george` quasiperiodic GP has three fixed hyperparameters based on the photometry data. The time series is divided into three sections for clarity. The GP mean (plus systemic offset) is denoted by the blue line, and the 1σ confidence interval on the GP is the light blue shaded region. The residuals are plotted beneath each panel, with an rms scatter of 0.45 m s^{-1}.

Table 4
Results of Our `george` GP Retrieval

Parameter	Units	GP-only		GP + One-planet		GP + Sinusoid	
a	m s^{-1}	$5.94^{+11.51}_{-1.43}$	(5.06)	$5.38^{+6.91}_{-0.70}$	(4.49)	$5.47^{+7.98}_{-0.80}$	(5.04)
λ_e	days	18.74*	*	*	*	*	*
P_{GP}	days	16.28*	*	*	*	*	*
λ_p	-	0.76*	*	*	*	*	*
s	m s^{-1}	$0.38^{+1.42}_{-0.20}$	(0.27)	$0.30^{+0.81}_{-0.10}$	(0.16)	$0.31^{+0.87}_{-0.11}$	(0.31)
γ	m s^{-1}	$-0.41^{+5.27}_{-4.89}$	(-0.41)	$-0.42^{+2.86}_{-2.84}$	(-0.70)	$-0.44^{+3.22}_{-3.11}$	(-0.60)
K_s	m s^{-1}	-	-	$0.63^{+1.19}_{-0.43}$	(4.02)	$0.59^{+1.18}_{-0.39}$	(2.53)
ϕ_0	rad.	-	-	$3.11^{+1.93}_{-1.87}$	(3.59)	$3.03^{+2.03}_{-1.85}$	(3.87)
P	days	-	-	$3.95^{+13.03}_{-2.64}$	(15.24)	$4.20^{+13.63}_{-3.00}$	(6.68)
ω	rad.	-	-	$3.06^{+2.01}_{-1.96}$	(3.90)	0*	*
e	-	-	-	$0.03^{+0.27}_{-0.03}$	(0.12)	0*	*
$\ln \mathcal{Z}$	-	-149.26 ± 0.15		-149.72 ± 0.06		-149.75 ± 0.18	
$\ln \mathcal{L}_{MAP}$	-	-139.80		-134.09		-135.81	
rms	cm s^{-1}	0.45		0.46		0.45	

Note. The three models correspond to GP-only (no planet), GP + one-planet, and GP + sinusoid (one planet, restricted w and e). Columns contain the median of the marginalized distribution of each sampled parameter, and uncertainties correspond to 16th and 84th percentiles. Values in parentheses " () " denote the maximum a posteriori (MAP). Asterisks " * " denote fixed values, either from conditioning GP hyperparameters on the photometry data, or from restricting the Keplerian to a circular orbit. Missing values " - " denote that the parameter is not used in the model. The bottom rows contain the log-evidences returned by the nested sampler, the log-likelihood of the MAP vector, and the rms of the residuals. Uncertainties on model evidences correspond to the standard deviation after five separate runs of the sampler.

However, the assumptions made are reasonable for a goal of understanding how consecutive nights of observation relates to stellar activity inferences for stars like HD 101501.

5.2. Cadence Simulation Results

The injected Keplerian is successfully recovered if the following criteria are met: first, the recovered semi-amplitude must be greater than $3\sigma_K$, where σ_K is the standard deviation of K_s draws made by the nested sampler; second, the fractional error on the period must be within 10%. We also check against 1.0027 day^{-1} aliases of the recovered period (Dawson & Fabrycky 2010; 1 day = 1.0027 sidereal day). Our injection + recovery analysis indicates that high observing cadence, consisting of several nights of consecutive observation, is
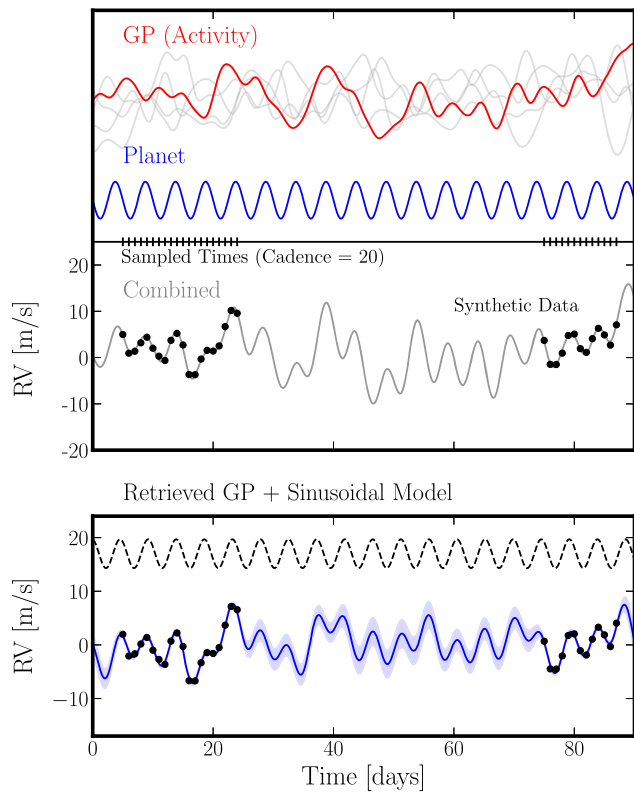
Figure 7. Illustration of the cadence analysis. The steps are as follows. (1) Generation of a synthetic RV data set, consisting of a GP draw (activity model, red curve in the top panel) and circular Keplerian (planet model, blue curve in the top panel; additional example GP draws are overplotted in gray). The two are added together and sampled at specific times based on the desired cadence. There are 33 samples in total. (2) Use of the GP framework to search for planet signals in the synthetic data set (details in Section 3). An example is shown in the bottom panel, including the GP + sinusoidal mean and 1σ confidence interval (blue line and shaded region) and the MAP Keplerian solution (dashed black line, offset for clarity). (3) Comparison between recovered orbital parameters and the true ones.

necessary for the GP framework to identify certain classes of exoplanets orbiting active stars. Figure 8 depicts the recovery of planets for a given cadence (green denotes success, whereas orange denotes convergence on an alias).

The 10, 20, and 33 day cadences have better completion across the parameter grid, especially for short periods. The observed cadence also has comparatively good completion, mostly due to there being 76 total timestamps (multiple per night) instead of 33. As expected, long-period/low-amplitude signals are difficult to recover for all cadences. We emphasize that this is not a full Monte Carlo analysis, and that unsuccessful retrievals at $K_s > 5\,\mathrm{m\,s^{-1}}$ and $P < 5$ days are likely a result of randomness in the GP draw and unfavorable sampling of the orbit. These high-amplitude Keplerians might be retrieved with a more careful analysis (e.g., selection of priors, more thorough posterior sampling, etc.). Planets with periods $\lesssim 1.5$ days are difficult to distinguish from their 1 day aliases, but are nevertheless recovered by the GP framework. Most modern RV analyses are prone to occasionally identifying aliases over true signals (Dumusque et al. 2017).

Importantly, the results show generally increasing completion with higher cadence. The 2 day cadence fails for nearly all cases except amplitudes $\gtrsim 5\,\mathrm{m\,s^{-1}}$, when the planet signal starts to rival the activity signal. The 5 day cadence exhibits

improvements, and the 33 day cadence shows the greatest completion of K_s and P combinations. There are diminishing returns going from the 10 day to 20 day cadence, and the 20 day to 33 day cadence. For short-period/low-amplitude planets ($K_s \lesssim 3\,\mathrm{m\,s^{-1}}$, $P \lesssim 5$ days), if sampling covers multiple orbital periods within a couple spot lifetimes, then the high-frequency Keplerian can be distinguished from the low-frequency GP/activity component. In this case the actual stellar rotation period may be irrelevant and alternative kernels such as the squared-exponential may be suitable for modeling the activity (Rajpaul et al. 2015). The most challenging planets ($K_s \lesssim 2\,\mathrm{m\,s^{-1}}$) are retrieved best by the highest cadences (20 days and 33 days). In these cases, the GP is capable of learning a repeated structure in the activity signal.

Given the above results, we would like to gauge whether the GP framework and EXPRES RVs of HD 101501 are actually sensitive to the full range of possible orbits specified by the priors. We perform a Monte Carlo analysis in which we repeat the injection/recovery procedure, sampled at the actual time-stamps of exposures, 10 times (i.e., we generate the bottom-right panel of Figure 8 an additional 10 times, each involving new GP draws). We group correct orbital periods and aliases together as successful recoveries. The results are shown in Figure 9. As expected the longest periods and smallest semi-amplitudes are most challenging to detect, as are periods at nearly 1 day. However, even for modest semi-amplitudes up to $\sim 3\,\mathrm{m\,s^{-1}}$, planets with periods less than a couple days are difficult to detect.

We explore two additional extensions to the above simulations. First, to what degree is detection reliant on the GP component? Second, how much easier is it to recover a planet with a known ephemeris (i.e., the planet transits)? These investigations involved modifying the underlying model to, in the first case, exclude a GP component and just fit a Keplerian, jitter term, and offset term. For the second case we use the full model, but all Keplerian parameters are fixed to their true values except for semi-amplitude. The results of these tests are shown in the Appendix. Without a GP, the sampler has much greater difficulty identifying planets in the simulated RV data sets. Given the simulated cadences, a GP is necessary to detect most planets with $K_s < 5$ m s^{-1}. While the sampler does identify Keplerians at $P \sim 15$ days, the retrievals might be falsely converging on the stellar activity signal given the similar stellar rotation period. In the future, it would be useful to explore the efficacy of GPs on RV data sets when the planet period is near the stellar rotation period. On the other hand, when the ephemeris is known and fixed a priori, we see a dramatic improvement in recovery when a GP is used. Robust detections are difficult for only the lowest semi-amplitudes and longest periods, limited by factors such as phase coverage, time baseline, and measurement uncertainty.

6. Discussion and Conclusions

We discuss some additional aspects of the data which were not thoroughly explored in the above GP analysis. For example, we have thus far neglected activity indicators (BIS, FWHM, etc.), and restricted attention to the high-fidelity photometry. Indeed, when simultaneous photometry is unavailable, indicators can become important in providing additional constraints on spot presence and evolution. We also analyze the photometry in greater detail by investigating each season's characteristics and performing light-curve inversion.
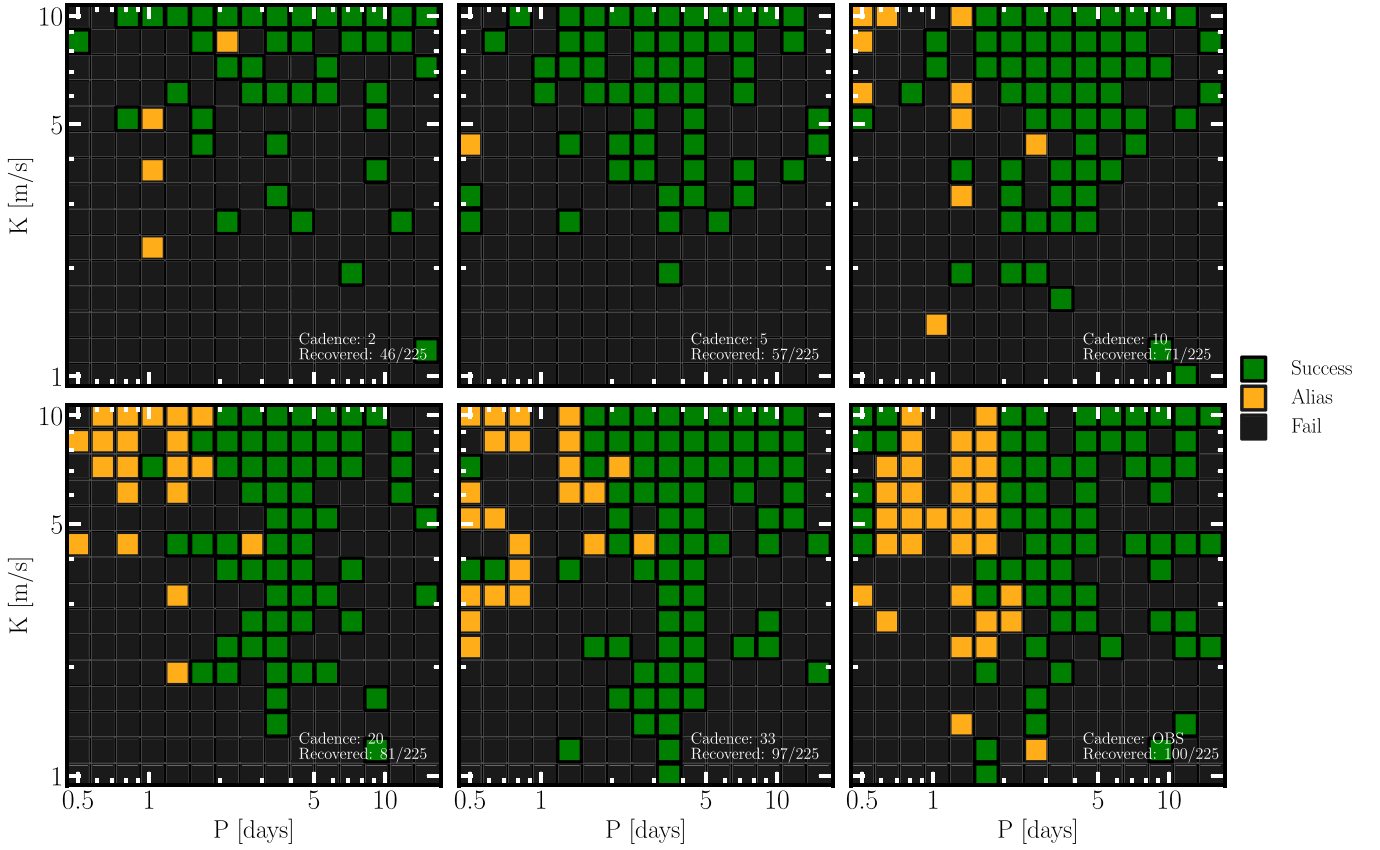
Figure 8. Results of the cadence analysis, in which the GP framework is applied to a synthetic RV time series, generated by a GP draw representing stellar activity and an added Keplerian. Each run involves a unique GP draw, and a combination of K_s and P drawn from a grid with log-uniform spacing. Green squares indicate successful recovery of the injected signal. Orange squares indicate recovery of an alias of the signal. Black squares indicate failure. The cadence stated in each plot (2, 5, 10, 20, and 33) denotes the number of consecutive nights of observation before a long gap in time, and the total number of data points is 33 in every run. The completion is generally higher for observing strategies using higher cadences. In particular, upwards of 10 consecutive nights of observing are needed to detect some short-period planets. For comparison, we also run the analysis on the epochs of our HD 101501 RV data set.
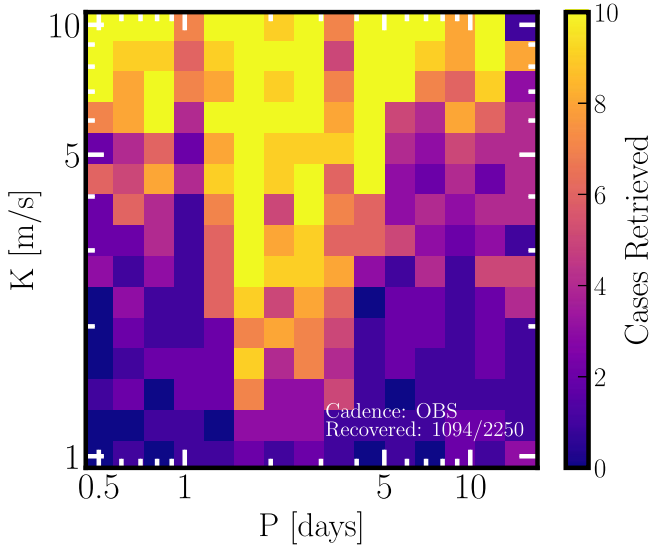
Figure 9. Sensitivity of the GP framework for identifying planets, given an observing cadence matching our HD 101501 data set. The GP framework is applied to a synthetic RV time series, generated by a GP draw representing stellar activity and an added Keplerian. Each run involves a unique GP draw, and a combination of K_s and P drawn from a grid with log-uniform spacing. The RV curve is then sampled at timestamps of EXPRES RV data. The color scale represents the number of successful retrievals after repeating the injection/recovery 10 times.

6.1. Activity Indicators

Several approaches directly incorporate indicators into the GP framework. Indicators may be modeled jointly with RVs as linear combinations of a single, latent GP and its derivative (Rajpaul et al. 2015; Jones et al. 2017; Gilbertson et al. 2020). Another method involves regression on RVs and an indicator time series where both GPs share certain hyperparameters (Suárez Mascareño et al. 2020) or, one can train a GP on an indicator time series and use the results as an initial guess for a subsequent RV analysis (Dumusque et al. 2017).

In Figure 10 we show the RV time series along with CCF FWHM, CCF BIS, and Hα equivalent width, as well as their generalized Lomb–Scargle periodograms (Scargle 1982; Zechmeister & Kürster 2009). The RV and BIS time series have power at the stellar rotation period, with BIS more pronounced. BIS shows a double-peaked structure, split between roughly the GP-derived rotation period and another peak near ∼17.2 days. This pattern is likely due to differential rotation, where long-lived spots at different latitudes exhibit different rotation periods. We attempted joint modeling of RVs and BIS with separate GPs that share λ_e, λ_p, and P_{GP}. Their likelihood functions were summed together. We sampled the BIS GP amplitude, mean, and jitter from similar distributions as used for the RVs. The zero-planet model is favored over the one-planet model, with $\ln \mathcal{Z}_0 = -363.98 \pm 0.07$ and
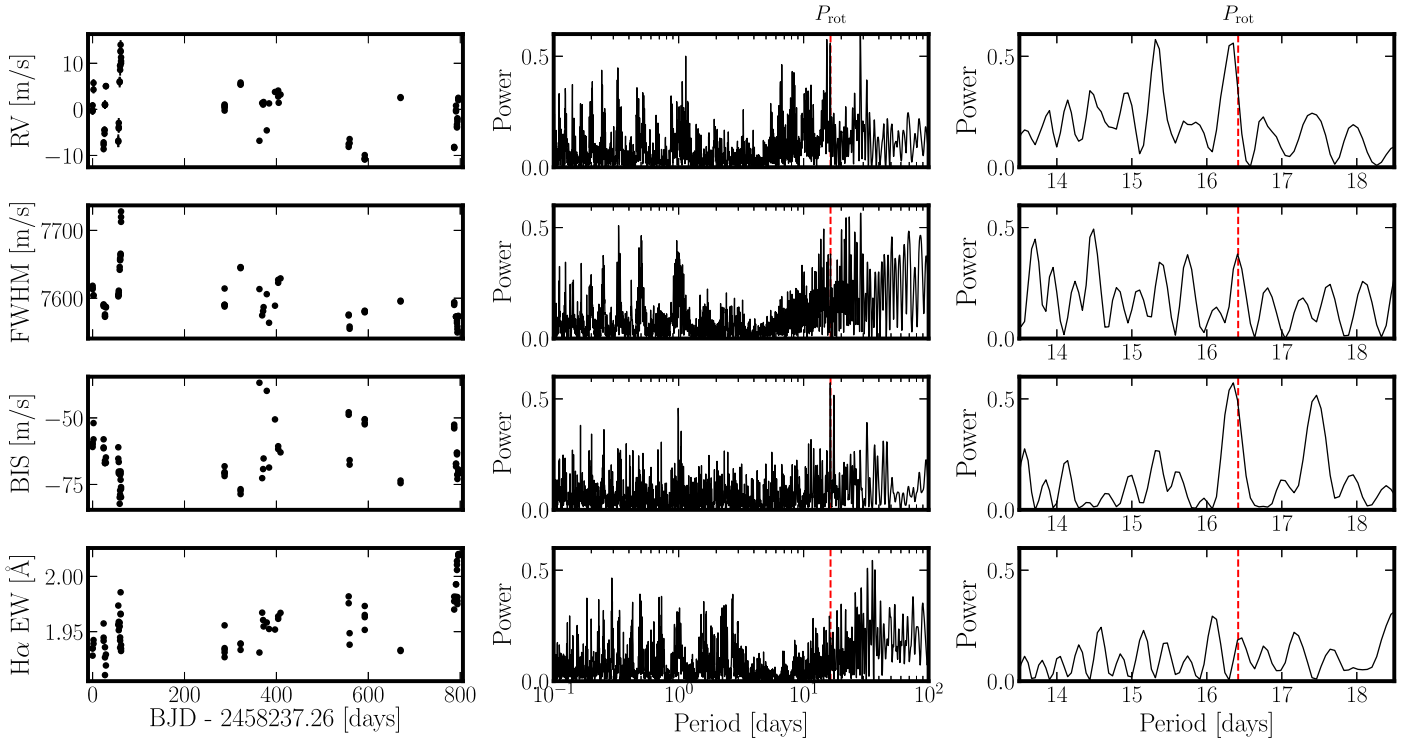
Figure 10. RV and activity indicator time series (left panels) and their periodograms (middle panels). The red dashed line denotes the stellar rotation period, as derived in this study. The periodograms are shown again in a cropped region around the stellar rotation period (right panels).

$\ln \mathcal{Z}_1 = -364.92 \pm 0.13$, respectively. The corresponding MAP values of P_{GP} are 15.87 days and 15.65 days, respectively, similar to the rotation period derived from RVs alone. The sampler converges to $\lambda_e = 34.01$ days and $\lambda_e = 27.47$ days for the two models, respectively. The APT light curve changes significantly between rotations, so the actual spot evolution is likely much faster than these estimates.

We make a few comments on the periodograms, which may simply be spurious features of the data set. The RV periodogram shows highest power at ~28 days; however, none of the GP models with planets converged to this orbital period in additional trials where we extended the orbital period prior to 40 days. Rather, they still tended toward the other peak at 15.3 days. Since the indicators do not have significant power at 15.3 days, a Keplerian might be responsible. However, we reiterate that the Bayesian evidence disfavors a planet in all of our fits (light-curve GP conditioning, BIS joint fitting, and freely fitting RVs), and 15.3 days is close to the stellar rotation period.

6.2. Photometric Variability

Our RV analysis warranted use of the most recent seasons of photometry. However, the remarkable 28 season baseline offers an opportunity to obtain more precise constraints on stellar rotation and activity. We again turn to GP regression, which has seen frequent applications toward inferring stellar properties and searching for transits in photometry (Vanderburg et al. 2015; Angus et al. 2018; Barros et al. 2020). We use a celerite GP with a covariance function given by Equation (5) and sample hyperparameters $\{B, C, L, P_{GP}\}$. We find a periodic timescale of $P_{GP} = 16.45^{+0.60}_{-0.51}$ days, and an evolutionary timescale of $L = 15.82^{+9.04}_{-3.07}$ days (uncertainties denote the 16th and 84th percentiles around the median). The MAP P_{GP} is 16.42 days, which we take as our best estimate of

the rotation period P_{rot}. Technically, this is probably not the equatorial rotation period. However, it is the period that best describes the data, and it might be influenced by the typical latitudes of spots. The GP with MAP hyperparameters is shown in the bottom panel of Figure 1. The evolutionary timescale L is consistent within 1σ of λ_e from our earlier analysis where we fit a george GP to the recent photometry. The periodic timescale P_{GP} also matches between the two fits. Formally, P_{GP} has a different definition in Equation (4) than it does in Equation (5), but it has similar meaning and influence on GP behavior. Their similarity gives some assurance that the stellar activity signal in the most recent three seasons shares similar characteristics with those of the whole baseline. The closeness of L and P_{rot} indicates that the spot distribution changes significantly between consecutive rotations, which also makes the light curve less coherent.

Some of our photometry seasons (e.g., 2001) have very coherent oscillations, while others (e.g., 1998) appear more random. We investigate inter-seasonal variations by fitting a celerite GP to each season individually. The GP provides, in theory, a more reliable estimate of the rotation period than the maximum power of the periodogram. The periodogram is based on a single sinusoid model and most clearly identifies a signal when the phase, amplitude, and period are constant. The quasiperiodic GP can accommodate signals that exhibit small departures from an overall phase, amplitude, and period, for example due to the appearance and disappearance of spots. However, the robustness of the GP is tied to the quantity and cadence of the data (lacking in 2017, for example). Also, if multiple modes are present within a given season, the GP learns a value that maximizes the likelihood, which might not actually be representative of any single mode. In 10 of 28 seasons the best-fit GP has $P_{GP} < 16$ days, reaching as low as 12–14 days. It is below 17 days in all cases. The variability in periodic
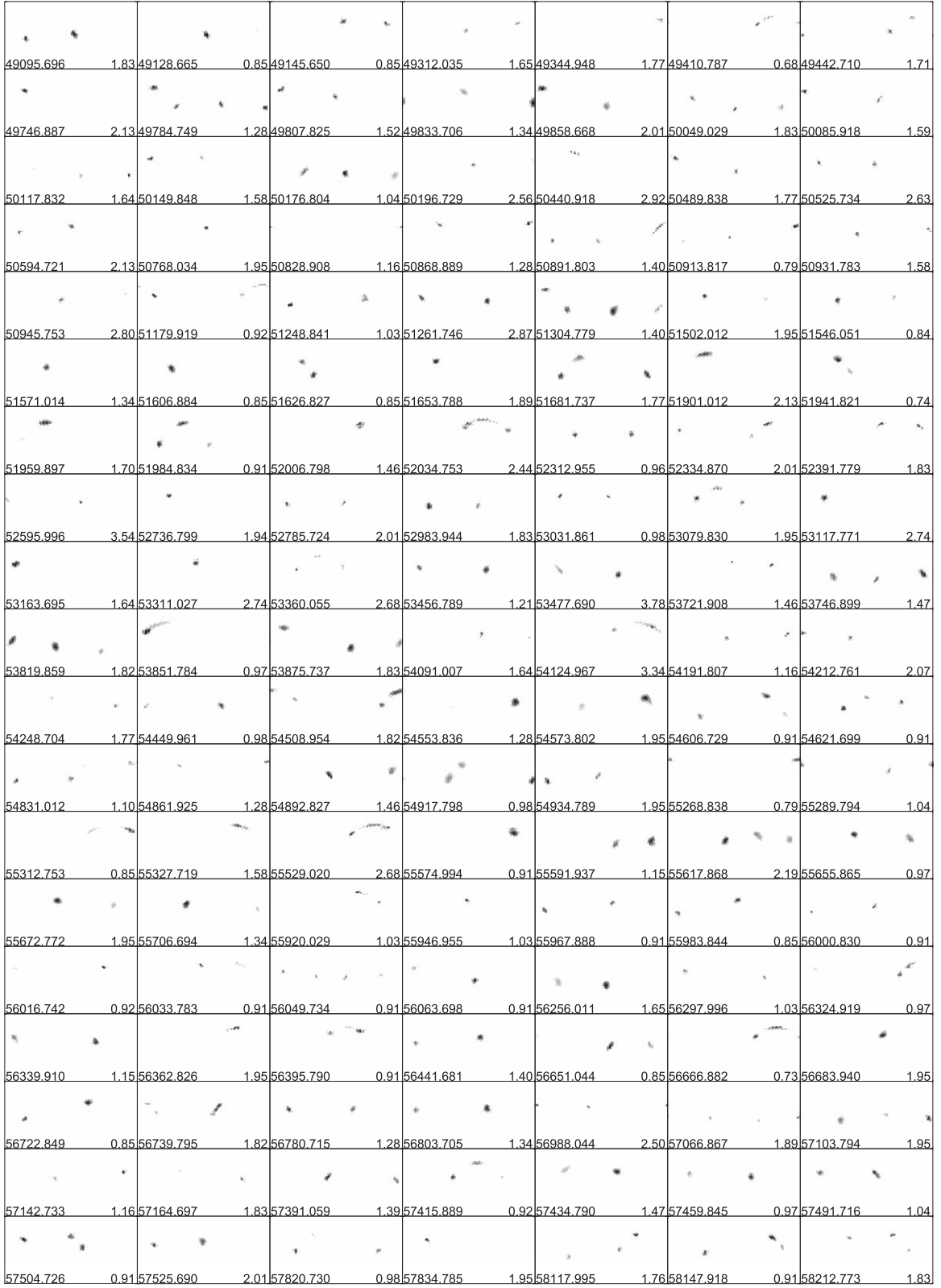
Figure 11. Pseudo-Mercator surfaces of HD 101501 reconstructed using LI. The date of the earliest data point used in the light curve are included in the lower left corner of each plot (JD-2,400,000.5). Each of the surfaces included here use data that were collected before the EXPRES data. The number of rotations used in each inversion is included in the lower right corner of each plot. Each plot shows all stellar longitudes horizontally and all stellar latitudes vertically. The center of the star, as visible to the observer, at phase 0.25 is located at 0° longitude, and at the left edge of the surfaces here. The star rotates over time with the longitudes decreasing.

timescales is most likely a sign of differential rotation. In a previous study, Mittag et al. (2017) analyze periodograms of Ca II H&K and Ca II IRT line strengths and find power at multiple periods, which they also attribute to differential rotation. We perform a bootstrap by sampling the 28 values of P_{GP} with replacement 10,000 times, recording the rotational

shear $\alpha = \Delta P/P$ at each iteration. The difference between maximum and minimum periods, ΔP, assumes that the maximum corresponds to rotation at the poles and the minimum at the equator. We find $\alpha = 0.45^{+0.03}_{-0.19}$, which is similar to the solar rotational shear of ~ 0.4 (Snodgrass & Ulrich 1990).

6.3. Light-curve Inversion

In order to better understand the evolution of the starspots on the surface of HD 101501, we applied a light-curve inversion algorithm to reconstruct the stellar surfaces. The algorithm light-curve inversion (LI; Harmon & Crews 2000) uses a modified Tikhonov regularization and stellar parameters to converge on a solution and makes no a priori assumptions about starspot shape, number, or size.

For the APT light curve, we divided the light curve into portions lasting approximately one rotation. When necessary to provide more phase coverage, the portion of the light curve used for inversion lasted more than one rotation (this is noted in the lower right corners in Figures 11 and 12). In very few cases, data points were used for overlapping portions of the light curve. For the TESS light curve, there is a gap over 4 days long in the middle of the sector of observation (see Figure 2). We divided the light curve during this time into two rotations and binned the data into bins 0.01 in phase. Both rotations observed with TESS have incomplete phase coverage.

We assigned $T_{\rm eff} = 5500$ K and a spot temperature of $T_{\rm spot} = 4500$ K, based on Figure 7 of Berdyugina (2005). Combining those temperatures and the appropriate response function for the filters yields a spot-to-photosphere ratio of 0.3452 for the V band and 0.4530 for the TESS observations. In addition to this value, LI also uses limb-darkening coefficients as input. For the V-band APT inversions, quadratic limb-darkening coefficients are used (0.5955 and 0.1488; Claret et al. 2013). For the TESS inversions, quadratic limb-darkening coefficients are also used (0.3876 and 0.2036; Claret 2018). Each inversion used a unique rms error in order to balance the inversion algorithm between overfitting and oversmoothing the data (the average rms for the APT light curves was 0.0013 and both TESS light curves used an rms of 0.0003). A stellar inclination of $i = 52°$ was found from the $v \sin i$ given by Brewer et al. (2016), the stellar diameter (Bonneau et al. 2006), and the parallax (Gaia Collaboration et al. 2018).

The reconstructed surfaces can be found in Figures 11 and 12. The reconstructed dark regions on the stellar surface are not necessarily individual starspots, but may be unresolved groups of spots. We cannot differentiate between these possibilities, and we refer to the dark regions as starspots. The starspots of HD 101501 behave similarly to sunspot groups in that they typically evolve on the same timescale as a rotation. On some occasions, the same spot appears to be present for more than one rotation. The latitudes at which the starspots appear are only weakly constrained by the light curve and the limb-darkening coefficients used. Because of this and the short starspot lifetimes, we do not further investigate differential rotation for this star. The variations in the photometric data and the resultant surface reconstructions indicate that at all points of observation, there is evidence of starspots on the surface. Furthermore, the surfaces that result from the inversion of TESS light curves show similar structures, but are not a direct comparison to the V-band reconstructions because the bandpasses are very different. The TESS filter covers a much larger
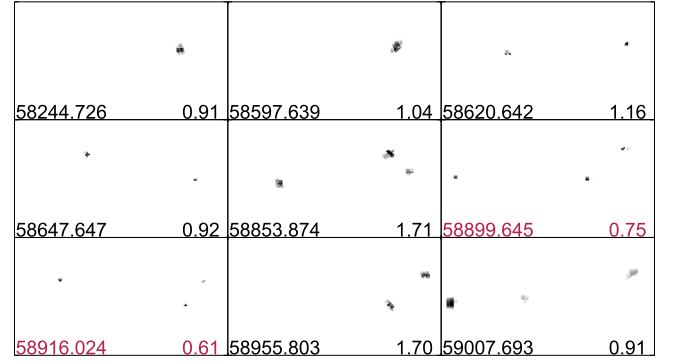

Figure 12. Pseudo-Mercator surfaces of HD 101501 reconstructed using LI, as in Figure 11. The surfaces here use photometric data obtained during the epochs of EXPRES data. The two surfaces with MJD and the number of rotations used in the inversion written in red are reconstructed from TESS data.

wavelength range, and the contrast between cool starspots and the photosphere is more dramatic at shorter wavelengths.

6.4. Conclusions

The Sun-like star HD 101501 presents an interesting case study for understanding stellar activity signatures in RVs and photometry. We present new high-precision RVs of HD 101501 along with simultaneous ground-based photometry with a baseline of 28 years. Several weeks of photometry from TESS are also analyzed. We summarize our findings as follows.

1. A GP framework is used to model both the photometry as well as the correlated noise in the RV time series. HD 101501 represents a case study for the GP framework that may be applied to RVs of other EXPRES targets. The RVs, which exhibit variations at a level of ~ 10 m s^{-1}, are best explained by an activity-only model. The Bayesian evidence disfavors the presence of a Keplerian signal in our data.

2. Through a simple injection and recovery analysis, we explore the space of orbital parameters to which the GP framework is sensitive. We test different cadences in order to understand how observing strategy impacts our ability to detect planets. The lowest cadences, in which exposures are largely spaced in time, contribute very little to the GP retrieval. Higher cadences, in which the star is observed for many consecutive nights, assist the GP framework in separating short-period orbits from the stellar activity signal. These results refine our observing plans and offer important guidance for RV observations of active stars.

3. GPs place tight constraints on the stellar rotation period associated with spots, at $P_{\rm rot} \sim 16.4$ days. We use GPs to analyze periodicity in individual photometric observing seasons. The variability from season to season suggests a rotational shear of ~ 0.45 and an equatorial rotation period of ~ 13 days.

4. Reconstructed stellar surfaces show the persistent presence of starspots on the surface of HD 101501 at all times. While starspots are always present, they are observed to change significantly between rotations making it impossible to trace their evolution over many rotations in these data.

Detecting exoplanets around active stars remains a significant challenge. Correlated noise models show great promise for mitigating activity in RVs, especially when combined with simultaneous photometry. GPs have had great success in modeling stellar activity in HARPS, HARPS-N, CARMENES, and ESPRESSO RVs, and this analysis of HD 101501 represents the first application of GPs to EXPRES RVs. The high precision of current spectrographs, optimized observing strategy, and new RV extraction techniques will push exoplanet detection limits in the near future.

Appendix

We include additional figures pertinent to the analysis of observing cadence and ground-based photometry. Figures 13 and 14 show results from the synthetic RV injection and recovery where a GP was excluded and where the period and phase were fixed, respectively. Figures 15 and 16 show APT photometry collected during individual seasons. GPs were fit to individual seasons to investigate variability, and place some constraint on the stellar rotational shear. RVs and activity indicators used in this study are listed in Table 5. Summary statistics regarding the APT photometry are presented in Table 6.
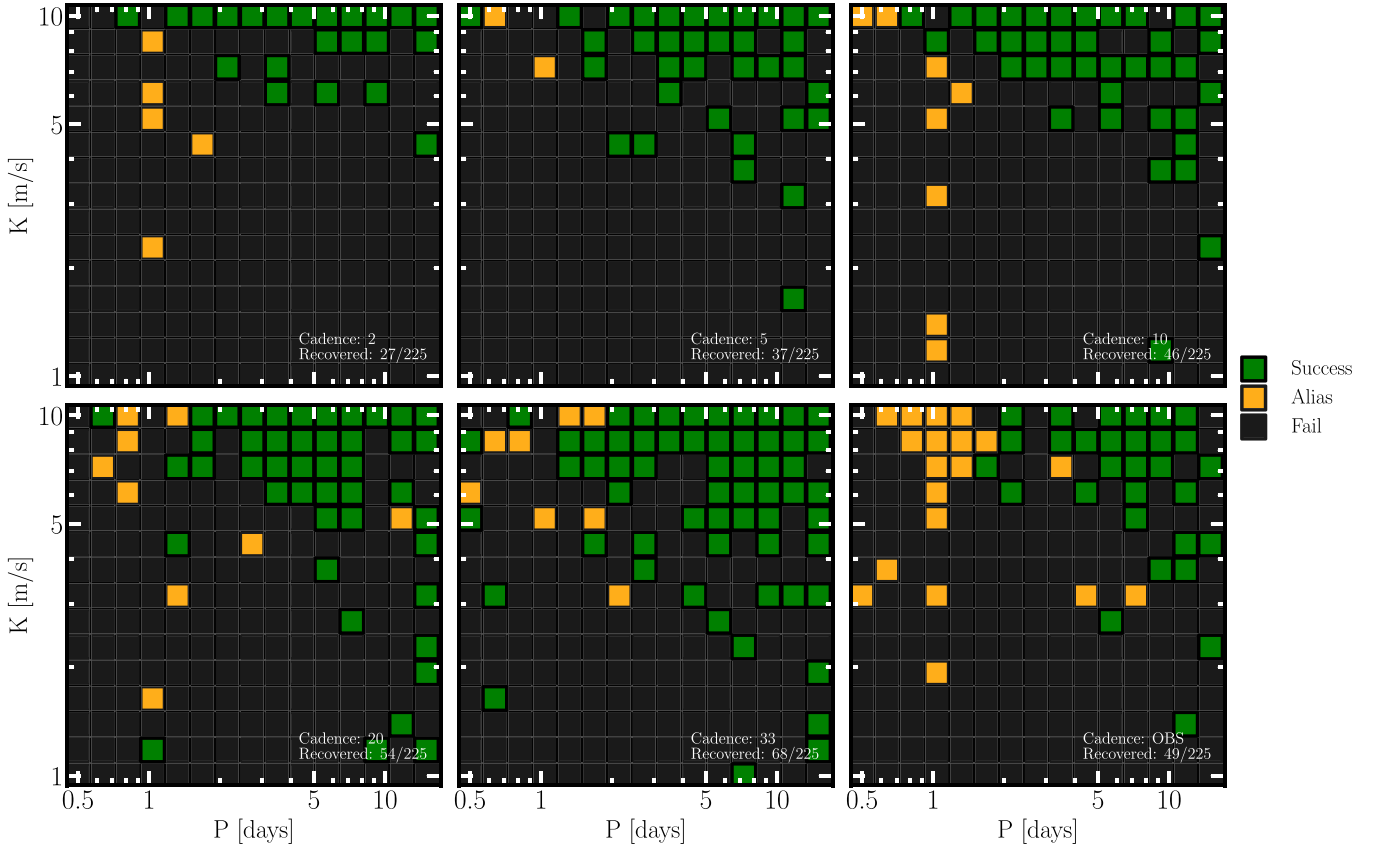

Figure 13. Same as Figure 8, except the model did not include a GP component. It included an offset term, jitter term, and sinuoid component. These simulations show significantly less completion compared to retrieval with the activity GP component.
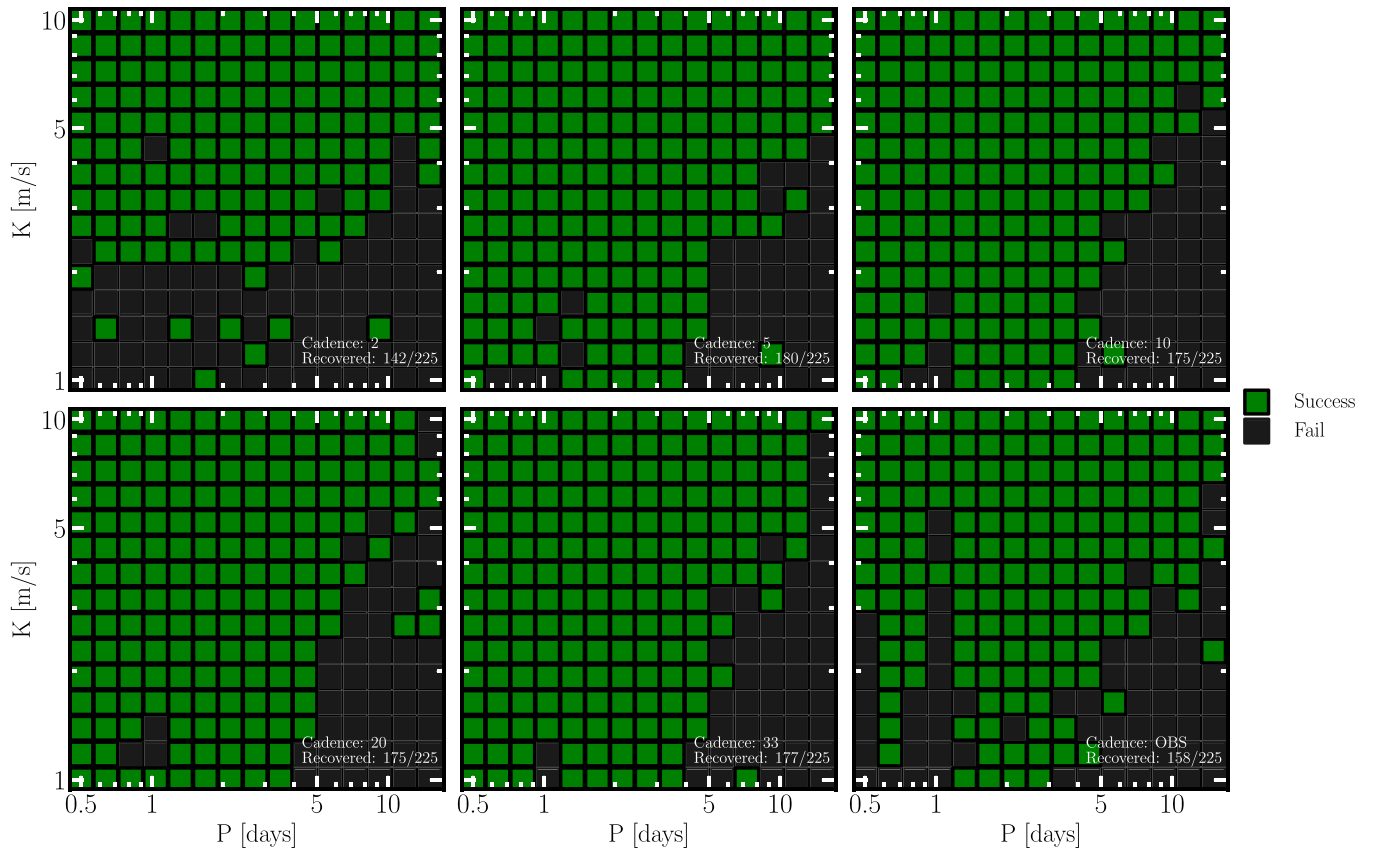
Figure 14. Same as Figure 8, except the model had period and phase fixed to true values. Such a model may be appropriate for real data when an ephemeris is known from the primary transit.
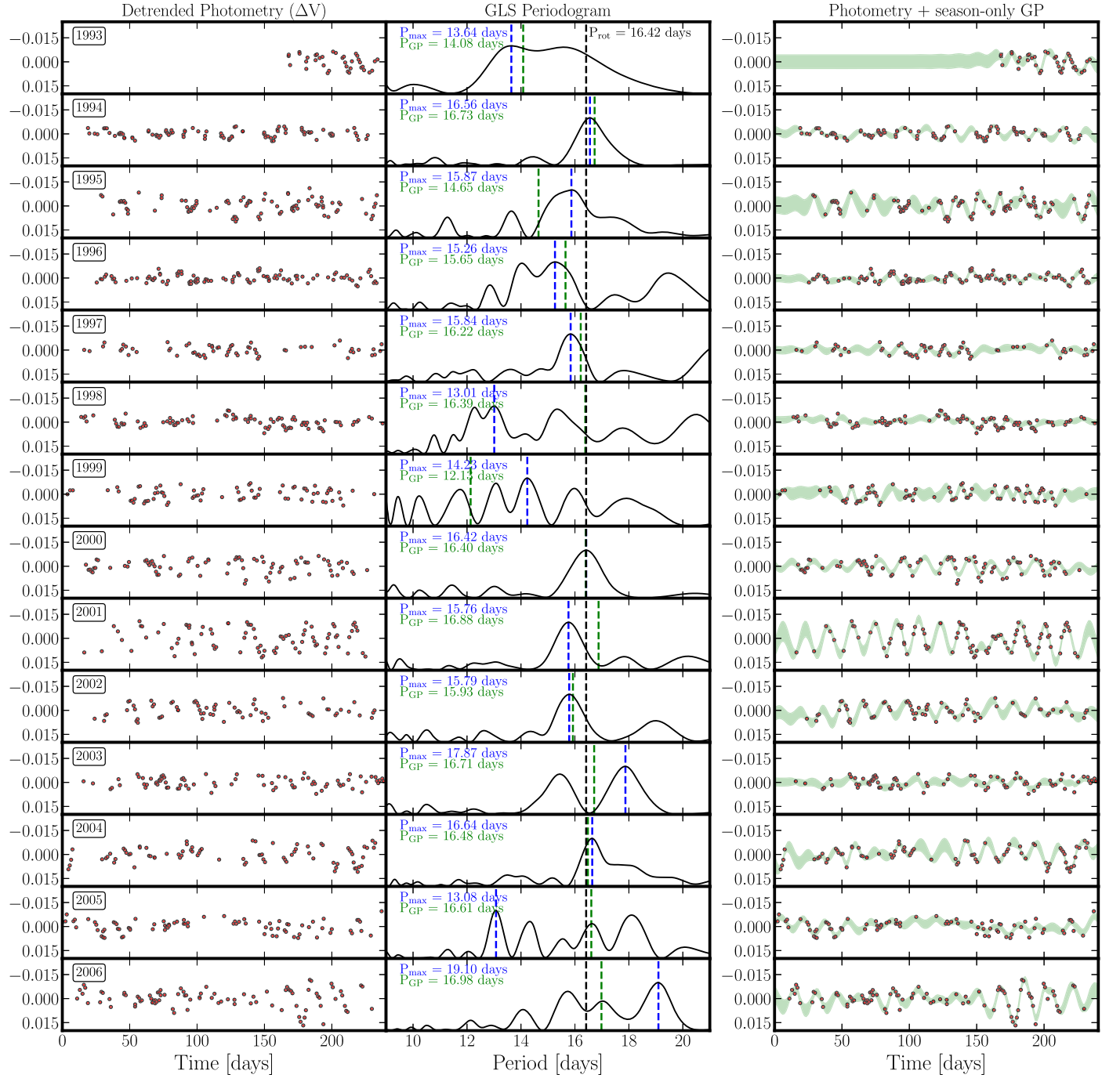
Figure 15. Analysis of individual APT photometry seasons (1993–2006). The left side of the figure shows the photometry data along with their generalized LS periodograms. The three periods marked are: (1) maxmimum power in the periodogram (blue); (2) the periodic timescale hyperparameter of a `celerite` GP, fit to that season of data (green); and (3) the rotation period of the star (black). The right panels show the `celerite` GP fit to each season (1σ confidence interval).
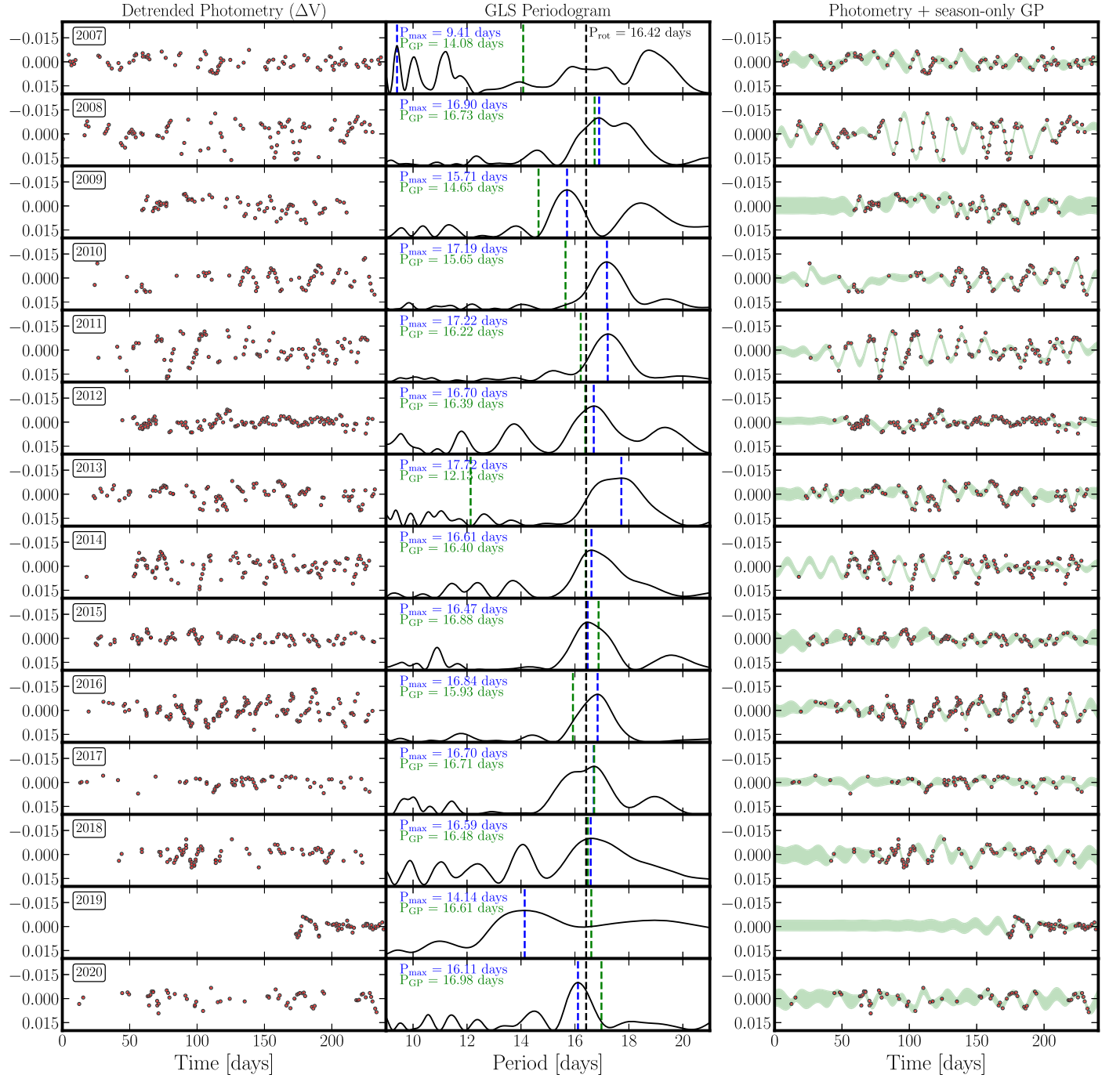
Figure 16. Analysis of individual APT photometry seasons (2007–2020). The left side of the figure shows the photometry data along with their generalized LS periodograms. The three periods marked are: (1) maxmimum power in the periodogram (blue); (2) the periodic timescale hyperparameter of a `celerite` GP, fit to that season of data (green); and (3) the rotation period of the star (black). The right panels show the `celerite` GP fit to each season (1σ confidence interval).

Table 5
RV Measurements and Activity Indicators

Time (JD-2,440,000)	Vel. (m s^{-1})	Unc. (m s^{-1})	Hα EW (Å)	BIS (m s^{-1})	CCF FWHM (m s^{-1})	Time (JD-2,440,000)	Vel. (m s^{-1})	Unc. (m s^{-1})	Hα EW (Å)	BIS (m s^{-1})	CCF FWHM (m s^{-1})
18237.2600	0.866	0.735	1.9347	−59.4	7613.3	18559.2685	5.829	0.340	1.9388	−76.7	7645.4
18237.2650	−0.183	0.809	1.9283	−60.9	7618.3	18559.2728	5.485	0.336	1.9393	−77.4	7645.8
18237.2690	−0.406	0.807	1.9351	−59.9	7615.2	18600.3138	−6.818	0.323	1.9311	−36.8	7613.4
18239.2394	4.284	0.838	1.9391	−51.9	7604.1	18606.3136	1.378	0.281	1.9672	−72.6	7574.6
18239.2441	5.736	0.821	1.9424	−58.0	7604.1	18608.3141	1.033	0.293	1.9605	−69.2	7580.9
18261.2177	−7.176	0.697	1.9574	−61.4	7589.8	18609.3433	1.598	0.335	1.9547	−65.2	7586.8
18261.2222	−8.618	0.686	1.9446	−61.0	7588.0	18616.2515	−4.564	0.314	1.9583	−39.8	7605.9
18261.2268	−7.653	0.691	1.9417	−58.0	7590.9	18621.2651	1.294	0.291	1.9524	−68.6	7563.7
18263.2070	−4.434	0.715	-	-	-	18634.1729	3.776	0.275	1.9519	−50.5	7588.9
18263.2117	−5.267	0.762	-	-	-	18641.1586	4.078	0.356	1.9639	−61.7	7627.1
18263.2193	−4.526	0.796	-	-	-	18641.1641	2.774	0.329	1.9616	−60.6	7622.7
18264.1671	0.977	0.847	1.9359	−67.0	7576.1	18642.1850	1.429	0.307	1.9246	-	-
18264.1717	1.105	0.899	1.9267	−66.0	7573.8	18646.1772	3.214	0.367	1.9670	−62.9	7629.2
18264.1762	0.932	0.813	1.9107	−66.9	7572.5	18794.5362	−8.143	0.372	1.9757	−47.8	7574.5
18266.1937	5.011	0.642	1.9293	−64.8	7587.4	18794.5393	−7.524	0.409	1.9819	−48.8	7575.8
18266.2010	5.070	0.650	1.9194	−66.8	7586.3	18796.5347	−6.448	0.375	1.9382	−67.5	7558.2
18293.1759	−7.014	1.204	1.9564	−65.3	7602.6	18796.5379	−7.336	0.383	1.9486	−65.8	7554.9
18293.1817	−6.800	1.374	1.9736	−61.0	7605.4	18829.4906	−10.890	0.354	1.9631	−50.4	7580.1
18294.1745	−4.139	0.959	1.9589	−66.5	7608.3	18829.4933	−9.922	0.378	1.9651	−52.4	7581.5
18294.1789	−3.846	0.911	1.9558	−70.1	7604.4	18829.4970	−10.811	0.380	1.9516	−51.9	7579.1
18294.1833	−2.942	1.071	1.9513	−70.8	7611.1	18829.5012	−10.594	0.384	1.9732	−50.7	7580.8
18296.1927	5.893	1.136	1.9582	−82.2	7641.9	18907.4231	2.478	0.343	1.9334	−73.5	7596.3
18296.1974	6.064	1.029	1.9547	−79.8	7646.1	18907.4275	2.647	0.316	1.9325	−74.5	7595.1
18297.1717	9.454	1.068	1.9420	−78.8	7658.6	19024.1584	−8.145	0.314	1.9775	−53.3	7592.6
18297.1763	9.517	1.226	1.9448	−71.4	7655.9	19024.1668	−8.378	0.328	1.9700	−52.5	7590.1
18297.1809	8.567	1.245	1.9355	−77.2	7656.5	19024.1751	−8.263	0.336	1.9817	−53.9	7594.0
18298.1707	12.705	1.004	1.9662	−70.8	7665.6	19028.1551	0.813	0.351	1.9815	−68.2	7572.7
18298.1752	12.527	0.998	1.9856	−73.2	7664.6	19028.1580	−0.437	0.346	1.9927	−67.1	7573.0
18298.1798	14.018	1.012	1.9657	−70.0	7662.8	19028.1613	−0.152	0.354	1.9929	−67.3	7572.6
18299.1760	10.011	0.912	1.9325	−76.6	7727.9	19030.1878	−3.715	0.436	2.0105	−63.7	7570.4
18299.1806	11.297	0.937	1.9346	−79.7	7719.7	19030.2002	−3.288	0.356	2.0058	−63.0	7563.4
18299.1852	10.481	0.967	1.9379	−75.9	7712.5	19030.2118	−3.930	0.368	2.0139	−63.0	7566.5
18524.4706	0.594	0.324	1.9312	−71.8	7589.8	19031.1579	−2.632	0.338	1.9813	−71.3	7558.4
18524.4840	0.340	0.756	1.9557	−68.1	7614.2	19031.1624	−1.930	0.337	1.9778	−71.2	7554.3
18524.4961	1.055	0.303	1.9337	−70.7	7590.5	19031.1666	−2.136	0.350	1.9749	−72.9	7549.4
18524.5017	0.873	0.313	1.9269	−70.8	7590.1	19033.1566	2.298	0.394	2.0191	−70.9	7573.2
18524.5078	−0.264	0.330	1.9351	−70.3	7587.6	19033.1585	2.511	0.389	2.0202	−69.3	7574.0
18559.2641	5.351	0.325	1.9335	−78.6	7644.2	19033.1622	1.977	0.361	2.0187	−70.0	7572.5

Note. Columns are: time of exposure, RV following subtraction of the mean, uncertainty on velocity, bisector span, CCF FWHM, and Hα equivalent width. Dashes ("-") indicate that the indicator could not be reliably measured.

Table 6
Summary of APT Photometric Observations for HD 101501

Observing Season (1)	N_{obs} (2)	Date Range (HJD-2,400,000) (3)	Sigma (mag) (4)	Seasonal Mean (mag) (5)	Period (days) (6)
1992–93	37	49095–49161	0.00435	−0.65220(71)	13.56
1993–94	96	49312–49519	0.00229	−0.65817(23)	16.70
1994–95	92	49687–49891	0.00464	−0.65316(48)	14.18
1995–96	102	50049–50256	0.00255	−0.65933(25)	13.82
1996–97	63	50404–50629	0.00284	−0.65756(36)	15.57
1997–98	90	50768–50991	0.00360	−0.65699(37)	16.55
1998–99	74	51123–51350	0.00397	−0.65383(46)	12.25
1999–00	82	51502–51710	0.00443	−0.65858(49)	16.46
2000–01	85	51866–52074	0.00711	−0.64380(77)	16.71
2001–02	72	52238–52461	0.00411	−0.65103(48)	15.73
2002–03	83	52595–52818	0.00309	−0.65225(34)	13.45
2003–04	84	52950–53190	0.00522	−0.65473(57)	16.39
2004–05	84	53311–53556	0.00443	−0.65415(48)	16.50
2005–06	92	53687–53905	0.00637	−0.65090(66)	16.75
2006–07	88	54046–54277	0.00509	−0.65208(54)	13.56
2007–08	93	54406–54636	0.00717	−0.65223(74)	16.70
2008–09	67	54831–54982	0.00711	−0.64735(87)	14.18
2009–10	67	55161–55368	0.00624	−0.63311(76)	13.82
2010–11	96	55529–55728	0.00735	−0.64932(75)	15.57
2011–12	125	55912–56097	0.00330	−0.65570(30)	16.55
2012–13	98	56256–56464	0.00513	−0.65605(52)	12.25
2013–14	108	56616–56825	0.00533	−0.65378(51)	16.46
2014–15	105	56988–57194	0.00289	−0.65929(28)	16.71
2015–16	146	57348–57558	0.00569	−0.65075(71)	15.73
2016–17	62	57707–57921	0.00288	−0.65625(71)	13.45
2017–18	77	58100–58281	0.00427	−0.65808(49)	16.39
2018–19	59	58597–58662	0.00309	−0.65696(40)	16.50
2019–20	63	58802–59022	0.00391	−0.65783(49)	16.75

ORCID iDs

Samuel H. C. Cabot ⓘ https://orcid.org/0000-0001-9749-6150
Rachael M. Roettenbacher ⓘ https://orcid.org/0000-0002-9288-3482
Gregory W. Henry ⓘ https://orcid.org/0000-0003-4155-8513
Lily Zhao ⓘ https://orcid.org/0000-0002-3852-3590
Debra A. Fischer ⓘ https://orcid.org/0000-0003-2221-0861
John M. Brewer ⓘ https://orcid.org/0000-0002-9873-1471
Joe Llama ⓘ https://orcid.org/0000-0003-4450-0368
Ryan R. Petersburg ⓘ https://orcid.org/0000-0003-2168-0191
Andrew E. Szymkowiak ⓘ https://orcid.org/0000-0002-4974-687X

References

Aigrain, S., Pont, F., & Zucker, S. 2012, MNRAS, 419, 3147
Ambikasaran, S., Foreman-Mackey, D., Greengard, L., Hogg, D. W., & O'Neil, M. 2015, ITPAM, 38, 252
Anglada-Escudé, G., Amado, P. J., Barnes, J., et al. 2016, Natur, 536, 437
Angus, R., Morton, T., Aigrain, S., Foreman-Mackey, D., & Rajpaul, V. 2018, MNRAS, 474, 2094
Barros, S. C. C., Demangeon, O., Díaz, R. F., et al. 2020, A&A, 634, A75
Benatti, S., Damasso, M., Desidera, S., et al. 2020, A&A, 639, A50
Berdyugina, S. V. 2005, LRSP, 2, 8
Blackman, R. T., Fischer, D. A., Jurgenson, C. A., et al. 2020, AJ, 159, 238
Boisse, I., Bouchy, F., Hébrard, G., et al. 2011, A&A, 528, A4
Bonneau, D., Clausse, J. M., Delfosse, X., et al. 2006, A&A, 456, 789
Boyajian, T. S., McAlister, H. A., van Belle, G., et al. 2012, ApJ, 746, 101
Brewer, J. M., Fischer, D. A., Blackman, R. T., et al. 2020, AJ, 160, 67
Brewer, J. M., Fischer, D. A., Valenti, J. A., & Piskunov, N. 2016, ApJS, 225, 32
Buchner, J., Georgakakis, A., Nandra, K., et al. 2014, A&A, 564, A125
Cegla, H. 2019, Geosc, 9, 114

Chaplin, W. J., & Miglio, A. 2013, ARA&A, 51, 353
Cincunegui, C., Díaz, R. F., & Mauas, P. J. D. 2007, A&A, 469, 309
Claret, A. 2018, A&A, 618, A20
Claret, A., Hauschildt, P. H., & Witte, S. 2013, A&A, 552, A16
Cloutier, R., Astudillo-Defru, N., Doyon, R., et al. 2017, A&A, 608, A35
Cretignier, M., Dumusque, X., Allart, R., Pepe, F., & Lovis, C. 2020, A&A, 633, A76
Davis, A. B., Cisewski, J., Dumusque, X., Fischer, D. A., & Ford, E. B. 2017, ApJ, 846, 59
Dawson, R. I., & Fabrycky, D. C. 2010, ApJ, 722, 937
Donahue, R. A., Saar, S. H., & Baliunas, S. L. 1996, ApJ, 466, 384
Dravins, D. 1982, ARA&A, 20, 61
Dumusque, X. 2018, A&A, 620, A47
Dumusque, X., Borsa, F., Damasso, M., et al. 2017, A&A, 598, A133
Dumusque, X., Pepe, F., Lovis, C., et al. 2012, Natur, 491, 207
Dumusque, X., Udry, S., Lovis, C., Santos, N. C., & Monteiro, M. J. P. F. G. 2011, A&A, 525, A140
Duquennoy, A., & Mayor, M. 1991, A&A, 500, 337
Espinoza, N., Brahm, R., Henning, T., et al. 2020, MNRAS, 491, 2982
Faria, J. P., Adibekyan, V., Amazo-Gómez, E. M., et al. 2020, A&A, 635, A13
Faria, J. P., Haywood, R. D., Brewer, B. J., et al. 2016, A&A, 588, A31
Feroz, F., & Hobson, M. P. 2008, MNRAS, 384, 449
Feroz, F., Hobson, M. P., & Bridges, M. 2009, MNRAS, 398, 1601
Feroz, F., Hobson, M. P., Cameron, E., & Pettitt, A. N. 2019, OJAp, 2, 10
Figueira, P., Santos, N. C., Pepe, F., Lovis, C., & Nardetto, N. 2013, A&A, 557, A93
Fischer, D. A., Anglada-Escude, G., Arriagada, P., et al. 2016, PASP, 128, 066001
Fischer, D. A., Marcy, G. W., & Spronck, J. F. P. 2014, ApJS, 210, 5
Fischer, D. A., & Valenti, J. 2005, ApJ, 622, 1102
Foreman-Mackey, D., Agol, E., Ambikasaran, S., & Angus, R. 2017, AJ, 154, 220
Gaia Collaboration, Brown, A. G. A., Vallenari, A., et al. 2018, A&A, 616, A1
Giguere, M. J., Fischer, D. A., Zhang, C. X. Y., et al. 2016, ApJ, 824, 150
Gilbertson, C., Ford, E. B., Jones, D. E., & Stenning, D. C. 2020, arXiv:2009.01085
Grunblatt, S. K., Howard, A. W., & Haywood, R. D. 2015, ApJ, 808, 127

Hall, D. S., & Henry, G. W. 1994, IAPPP, 55, 51

Hall, R. D., Thompson, S. J., Handley, W., & Queloz, D. 2018, MNRAS, 479, 2968

Harmon, R. O., & Crews, L. J. 2000, AJ, 120, 3274

Haywood, R. D., Collier Cameron, A., Queloz, D., et al. 2014, MNRAS, 443, 2517

Henry, G. W. 1999, PASP, 111, 845

Howard, A. W., & Fulton, B. J. 2016, PASP, 128, 114401

Jeffers, S. V., Dreizler, S., Barnes, J. R., et al. 2020, Sci, 368, 1477

Johnson, H. L., & Morgan, W. W. 1953, ApJ, 117, 313

Jones, D. E., Stenning, D. C., Ford, E. B., et al. 2017, arXiv:1711.01318

Jurgenson, C., Fischer, D., McCracken, T., et al. 2016, Proc. SPIE, 9908, 99086T

Kass, R. E., & Raftery, A. E. 1995, J. Am. Stat. Assoc., 90, 773

Kosiarek, M. R., & Crossfield, I. J. M. 2020, AJ, 159, 271

Levine, S. E., Bida, T. A., Chylek, T., et al. 2012, Proc. SPIE, 8444, 844419

Meunier, N., & Lagrange, A. M. 2013, A&A, 551, A101

Mittag, M., Hempelmann, A., Schmitt, J. H. M. M., et al. 2017, A&A, 607, A87

Nelson, B. E., Ford, E. B., Buchner, J., et al. 2020, AJ, 159, 73

Pepe, F., Cristiani, S., Rebolo, R., et al. 2013, Msngr, 153, 6

Petersburg, R. R., Ong, J. M. J., Zhao, L. L., et al. 2020, AJ, 159, 187

Queloz, D., Bouchy, F., Moutou, C., et al. 2009, A&A, 506, 303

Queloz, D., Henry, G. W., Sivan, J. P., et al. 2001, A&A, 379, 279

Quirrenbach, A., Amado, P. J., Mandel, H., et al. 2010, Proc. SPIE, 7735, 773513

Rajpaul, V., Aigrain, S., Osborne, M. A., Reece, S., & Roberts, S. 2015, MNRAS, 452, 2269

Rajpaul, V., Buchhave, L. A., & Aigrain, S. 2017, MNRAS, 471, L125

Rasmussen, C. E., & Williams, C. K. I. 2006, Gaussian Processes for Machine Learning (Cambridge, MA: MIT Press), https://mitpress.mit.edu/books/gaussian-processes-machine-learning

Ricker, G. R., Winn, J. N., Vanderspek, R., et al. 2014, Proc. SPIE, 9143, 914320

Robertson, P., Stefansson, G., Mahadevan, S., et al. 2020, ApJ, 987, 125

Roettenbacher, R. M., & Vida, K. 2018, ApJ, 868, 3

Saar, S. H., Butler, R. P., & Marcy, G. W. 1998, ApJL, 498, L153

Scargle, J. D. 1982, ApJ, 263, 835

Schrijver, C. J., & Zwaan, C. 2000, Solar and Stellar Magnetic Activity (Cambridge: Cambridge Univ. Press), 63

Snodgrass, H. B., & Ulrich, R. K. 1990, ApJ, 351, 309

Suárez Mascareño, A., Faria, J. P., Figueira, P., et al. 2020, A&A, 639, A77

Toner, C. G., & Gray, D. F. 1988, ApJ, 334, 1008

Tuomi, M., Jones, H. R. A., Jenkins, J. S., et al. 2013, A&A, 551, A79

Valenti, J. A., & Fischer, D. A. 2005, ApJS, 159, 141

Vanderburg, A., Montet, B. T., Johnson, J. A., et al. 2015, ApJ, 800, 59

Zechmeister, M., & Kürster, M. 2009, A&A, 496, 577